AGU PUBLICATIONS

JGR

Journal of Geophysical Research: Solid Earth

RESEARCH ARTICLE
10.1002/2015JB012510

Key Points:
- We quantitatively compare changes in seismicity at The Geysers, Salton Sea, and Coso geothermal fields
- Fluid injection drives seasonal seismicity rate transients at The Geysers but not Salton Sea or Coso
- Each field exhibits significant changes in b value, magnitude distribution, and depth distribution

Correspondence to:
D. T. Trugman,
dtrugman@ucsd.edu

Citation:
Trugman, D. T., P. M. Shearer, A. A. Borsa, and Y. Fialko (2016), A comparison of long-term changes in seismicity at The Geysers, Salton Sea, and Coso geothermal fields, *J. Geophys. Res. Solid Earth*, *121*, 225–247, doi:10.1002/2015JB012510.

Received 9 SEP 2015
Accepted 25 DEC 2015
Accepted article online 7 JAN 2016
Published online 23 JAN 2016

A comparison of long-term changes in seismicity at The Geysers, Salton Sea, and Coso geothermal fields

Daniel T. Trugman[1], Peter M. Shearer[1], Adrian A. Borsa[1], and Yuri Fialko[1]

[1]Institute of Geophysics and Planetary Physics, Scripps Institution of Oceanography, La Jolla, California, USA

Abstract Geothermal energy is an important source of renewable energy, yet its production is known to induce seismicity. Here we analyze seismicity at the three largest geothermal fields in California: The Geysers, Salton Sea, and Coso. We focus on resolving the temporal evolution of seismicity rates, which provides important observational constraints on how geothermal fields respond to natural and anthropogenic loading. We develop an iterative, regularized inversion procedure to partition the observed seismicity rate into two components: (1) the interaction rate due to earthquake-earthquake triggering and (2) the smoothly varying background rate controlled by other time-dependent stresses, including anthropogenic forcing. We apply our methodology to compare long-term changes in seismicity to monthly records of fluid injection and withdrawal. At The Geysers, we find that the background seismicity rate is highly correlated with fluid injection, with the mean rate increasing by approximately 50% and exhibiting strong seasonal fluctuations following construction of the Santa Rosa pipeline in 2003. In contrast, at both Salton Sea and Coso, the background seismicity rate has remained relatively stable since 1990, though both experience short-term rate fluctuations that are not obviously modulated by geothermal plant operation. We also observe significant temporal variations in Gutenberg-Richter *b* value, earthquake magnitude distribution, and earthquake depth distribution, providing further evidence for the dynamic evolution of stresses within these fields. The differing field-wide responses to fluid injection and withdrawal may reflect differences in in situ reservoir conditions and local tectonics, suggesting that a complex interplay of natural and anthropogenic stressing controls seismicity within California's geothermal fields.

1. Introduction

Recent technological developments have vastly expanded our capacity to exploit new sources of energy from beneath Earth's surface. At the same time, there is a rising level of public and scientific concern over seismicity induced by the anthropogenic stresses from energy production [*National Resource Council*, 2013; *Ellsworth*, 2013; *Weingarten et al.*, 2015]. In recent years, fluid injection and withdrawal at oil and gas production facilities are thought to have triggered earthquakes in a number of states within the central and eastern United States, including Oklahoma [*Keranen et al.*, 2013, 2014], Texas [*Frohlich et al.*, 2011; *Frohlich and Brunt*, 2013], Ohio [*Kim*, 2013], Colorado [*Ake et al.*, 2005], Arkansas [*Horton*, 2012], and New Mexico [*Rubinstein et al.*, 2014]. Two primary physical mechanisms related to fluid injection and withdrawal can account for this induced seismicity. Fluid fluxes from injection and withdrawal can directly increase the local pore pressure, which reduces the effective normal stress on nearby faults and hence pushes them closer to failure [*Hubbert and Rubey*, 1959; *Healy et al.*, 1968; *Raleigh et al.*, 1976]. Fluid injection and withdrawal can also modify the local stress state in the solid host rock through poroelastic coupling [*Biot*, 1941], which under certain conditions can trigger earthquakes [*Segall*, 1989; *Suckale*, 2009; *Segall and Lu*, 2015], and more generally can create poroelastic stresses at considerable distances from production and injection wells [*Segall et al.*, 1994]. Through these mechanisms—direct pore pressure increase and poroelastic stressing—both fluid injection and withdrawal can lead to induced seismicity in regions subject to intense oil and gas production, such as the central and eastern United States.

California has a high ambient rate of natural (tectonic) earthquakes, which makes distinguishing between natural and induced seismicity a less straightforward task than in the central and eastern United States, where the natural seismicity rate is low [*Goebel*, 2015]. In addition to hosting the extensive conventional oil and gas production fields of California's Kern County, San Joaquin Valley, and Los Angeles Basin, the state also

accounts for more than 80% of geothermal energy production within the United States [*Geothermal Energy Association*, 2013]. Geothermal fields like The Geysers, Salton Sea, and Coso are among the world's largest [*Matek and Gawell*, 2014]. As in conventional oil and gas production, geothermal energy production requires the extraction of fluids from the subsurface, and the resulting local changes in pore pressure and poroelastic stresses can trigger earthquakes [*Deichmann and Giardini*, 2009; *Brodsky and Lajoie*, 2013]. In geothermal fields, however, a third mechanism — thermoelastic stresses from fluid fluxes within hot geothermal reservoirs [*Segall and Fitzgerald*, 1998; *Majer and Peterson*, 2007] — can also induce seismicity. And while it is common practice to replenish overexploited geothermal reservoirs through fluid injection, failure to maintain a net fluid balance between injection and withdrawal can result in volumetric contraction within the reservoir, causing the surface to subside locally [*Mossop and Segall*, 1997; *Fialko and Simons*, 2000] and generating substantial poroelastic stresses at remote distances [*Trugman et al.*, 2014]. These differences make it uncertain whether insights gained from studies of induced seismicity within the central and eastern United States will generalize to the geothermal fields of California.

This study focuses on long-term changes in seismicity within the three largest geothermal fields in California: (1) The Geysers, located in Sonoma and Lake Counties to the north of San Francisco, (2) Salton Sea Geothermal Field, located in Imperial county in southeastern California, and (3) Coso Geothermal Field, located in Inyo county in eastern California. Induced seismicity has been previously studied at The Geysers [*Mossop and Segall*, 1997; *Majer and Peterson*, 2007; *Martinez-Garzon et al.*, 2014], Salton Sea [*Brodsky and Lajoie*, 2013], and Coso [*Feng and Lees*, 1998; *Fialko and Simons*, 2000; *Schoenball et al.*, 2015] geothermal fields, each in isolation. Our aim in this study is to provide a quantitative comparison of the temporal evolution of seismicity within these three prominent California geothermal fields, each with distinct local tectonics, reservoir conditions, and histories of energy production. In so doing, we hope to better understand the extent to which the production of geothermal energy, a nominally renewable energy source with tremendous potential for expansion in California [*Monastero*, 2002; *Adams*, 2011; *Matek and Gawell*, 2014], influences local seismicity, and by extension, local seismic hazard.

This manuscript is organized as follows. We begin by describing our methodology for estimating the time-varying background seismicity rate in each geothermal field. This is an essential step in our analyses, as the total observed seismicity rate is highly sensitive to coseismic stress changes from earthquake-earthquake interactions (most notably, aftershock sequences) that are unrelated to energy production. In brief, we use an Epidemic Type Aftershock Sequence (ETAS) framework [*Ogata*, 1988] to separate the total seismicity rate into two components: (1) the expected seismicity rate due to earthquake interaction and coseismic stresses (parameterized using the ETAS model) and (2) the time-varying background seismicity rate driven by fluctuations in anthropogenic and tectonic stresses. The generality of the method allows for its application to study seismicity rate changes in a variety of contexts and hence is described in some detail. We next apply our methodology to each of the three geothermal fields in turn, comparing the temporal evolution of seismicity rates, as well as earthquake magnitude and depth distributions, to monthly records of fluid injection and withdrawal. At The Geysers, we find that the background seismicity rate is strongly correlated with the monthly rate of fluid injection, and we observe significant temporal changes in Gutenberg-Richter b value, magnitude distribution, and depth distribution of earthquakes within the field. At both the Salton Sea and Coso geothermal fields, however, we find that the background seismicity rate is strongly correlated with fluid injection and withdrawal only during the early years of field operation (before 1990). We further observe temporal variations in b value and in the magnitude and depth distributions of earthquakes at the Salton Sea and Coso that may in part be the consequence of geothermal field operation but are also likely controlled by natural tectonic processes. We conclude our study with a comparison of the temporal evolution of seismicity in each field and discuss how our results contribute to the current understanding of induced seismicity in a broader context.

2. Methods and Description of Seismicity Rate Model

2.1. Background on ETAS Modeling

Our methodology for computing time variations in seismicity rate is based upon the Epidemic Type Aftershock Sequence (ETAS) model [*Ogata*, 1988]. In the ETAS model, earthquake occurrence within a region is modeled as a nonhomogeneous Poisson process with a total seismicity rate function, $\lambda(t)$, that is the sum of two terms: the background seismicity rate μ, assumed constant in time, and an interaction term $\nu(t)$ that represents the expected seismicity rate increase and subsequent decay characteristic of aftershock sequences [*Omori*, 1894;

Utsu, 1961]. The latter term is typically defined using a point process model [*Daley and Vere-Jones*, 2003] in which each observed earthquake generates a step increase in seismicity rate that decays with time following a modified Omori law [*Utsu et al.*, 1995]. With this parameterization, the ETAS model for seismicity rate then takes the form:

$$\lambda(t) = \mu + \nu(t) = \mu + \sum_{i;\, t > t_i} \frac{K\, 10^{\alpha(M_i - M_c)}}{(t - t_i + c)^p}, \tag{1}$$

where t_i and M_i are the occurrence time and magnitude of the ith earthquake, K and α are aftershock productivity parameters, p and c are Omori decay parameters, and M_c is the magnitude of completion (above which the seismicity rate is computed). Thus, for an observed catalog of earthquakes (t_i, M_i) and assumed magnitude of completion M_c, the standard ETAS model of seismicity rate is fully parameterized by five constants: μ, K, α, p, and c. Alternative forms of the ETAS model include additional free parameters related to the expected spatial dependence of aftershock earthquake clustering [*Ogata*, 2004]. We use the space-independent formulation presented above because it is more appropriate for studying field-wide changes in seismicity, especially in the absence of reliable estimates for the spatial anisotropy in the coseismic stresses that trigger aftershock activity based on earthquake catalog information alone [*Marsan and Lengliné*, 2010].

The optimal set of ETAS parameters $\theta = \{\mu, K, \alpha, p, c\}$ is region specific, and the parameter values are typically estimated by maximizing the likelihood of the observed earthquake data [*Ogata*, 1983, 1992]. This is equivalent to minimizing the negative log likelihood [*Daley and Vere-Jones*, 2003], which for the ETAS model can be written as

$$\mathrm{NLL}(\theta) = -\left[\sum_{i;\, T_0 < t_i < T_1} \log \lambda(t_i \mid \theta)\right] + \int_{T_0}^{T_1} \lambda(t \mid \theta)\mathrm{d}t, \tag{2}$$

where T_0 and T_1 denote the temporal limits of the observation interval for the earthquake catalog. In practice, the minimization of (2) can be implemented by any of a number of numerical optimization routines [*Press*, 2007]. However, since the rate function $\lambda(t)$ at time t is conditionally dependent on the history of earthquake occurrence (all events with $t_i < t$), the starting time of the observation interval T_0 should be chosen to be some time well after the first observed events in order to obtain unbiased parameter estimates [*Ogata*, 1992].

2.2. Temporal Variations in the Background Seismicity Rate

In the standard form of the ETAS model (described in the preceding subsection), the background seismicity rate μ is a constant that is independent of time. Thus, in this model the entire time dependence in the seismicity rate function $\lambda(t)$ (equation (1)) is due to earthquake-earthquake triggering, or equivalently, coseismic stress changes. However, transient stresses from processes unrelated to earthquake interaction, including anthropogenic forcing [*Nicholson and Wesson*, 1992; *Keranen et al.*, 2014; *Weingarten et al.*, 2015] and aseismic fault slip [*Toda et al.*, 2002; *Lohman and McGuire*, 2007; *Llenos et al.*, 2009], can cause time-dependent changes in seismicity rate. These changes in seismicity can be encompassed in a generalized ETAS framework by allowing the background rate to vary with time: $\mu = \mu(t)$ [*Marsan et al.*, 2013; *Kumazawa and Ogata*, 2013].

One problem with this more generalized formulation of ETAS is that there is no straightforward way to estimate $\mu(t)$ without making additional assumptions. Recall that for μ constant, the best fitting ETAS parameters can be estimated by minimizing the negative log likelihood of the observed data (t_i, M_i), as in equation (2). While the negative log likelihood (2) is a highly nonlinear function of (t_i, M_i), given enough data ($N \gg 5$), the five ETAS parameters can be stably estimated. However, if μ is allowed to vary with time, the estimation procedure becomes highly unstable, as a truly continuous $\mu(t)$ has an infinite number of free parameters [*Snyder and Miller*, 1991]. In essence, the data can be overfit by allowing $\mu(t)$ to become an arbitrarily rough function of time.

Our algorithm for computing the time-varying background seismicity rate $\mu(t)$ makes the physically plausible assumption that rate changes due to aseismic stresses and field-wide, anthropogenic forcing occur smoothly with time compared to the intense, step-like changes in seismicity rate characteristic of aftershock sequences. We thus impose a smoothness criterion, or regularization, on the background rate term $\mu(t)$ and seek to obtain the smoothest estimate of the time-varying background rate $\mu(t)$ that fits the data acceptably well. In doing so, we may lose resolution on very rough (short-term) fluctuations in background rate, but we ensure that any fluctuations that do appear in our inferred background rate are truly required by the observed data.

2.3. Regularized Inversion Algorithm

The seismicity rate model we employ is parameterized in terms of a background rate function $\mu(t)$ (nominally a continuous function of time) and a set θ_{ETAS} of ETAS parameters $[K, \alpha, p, c]$. To estimate the model parameters for a given catalog of events (t_i, M_i), we proceed as follows. We discretize $\mu(t)$ into N_μ entries, uniformly spaced in time with spacing Δt. Denoting this discretized rate function $\boldsymbol{\mu}$, we now wish to infer parameter values for the $N_\mu + 4$ entries in the parameter vector $\boldsymbol{\theta} = [\,\boldsymbol{\mu},\, K,\, \alpha,\, p,\, c\,]$. To do so, rather than minimize the negative log likelihood function as in (2), we minimize a penalized negative log likelihood function [*Good and Gaskins*, 1971; *Kumazawa and Ogata*, 2013] of the form:

$$\Psi(\boldsymbol{\theta}) = \text{NLL}(\boldsymbol{\theta}) + \gamma \cdot \Phi(\boldsymbol{\mu}), \tag{3}$$

where $\text{NLL}(\boldsymbol{\theta})$ refers to the negative log likelihood defined in (2), $\Phi(\boldsymbol{\mu})$ is a roughness penalty function, and γ is a regularization parameter that weights the relative importance between minimizing data misfit (NLL) and model roughness (Φ). The regularization stabilizes the parameter estimation procedure and prevents the inferred background rate $\boldsymbol{\mu}$ from becoming overly rough. For the purposes of this study, we use a first-derivative roughness norm as our penalty function:

$$\Phi(\boldsymbol{\mu}) = \sum_{j=1}^{N_\mu - 1} \left(\frac{\mu_{j+1} - \mu_j}{\Delta t} \right)^2 \Delta t. \tag{4}$$

We choose the regularization parameter γ by finding the value of γ that minimizes the effective Akaike Information Criteria (AIC) [*Akaike*, 1974] of the model:

$$\text{AIC}(\boldsymbol{\theta}) = 2\,\kappa(\boldsymbol{\theta}) + 2\,\text{NLL}(\boldsymbol{\theta}), \tag{5}$$

where the effective model degrees of freedom κ is estimated from the model roughness Φ (equation (4)). Conceptually, the AIC criterion provides a quantitative assessment of model fit, with the minimum value corresponding to a theoretically optimal balance between effective model degrees of freedom (κ) and data misfit (NLL) [*Akaike*, 1974]. However, the results presented here are not highly sensitive to the exact choice of γ, which can be chosen by a number of other standard approaches in inverse theory, including L-curve optimization or application of the discrepancy principle [*Snyder and Miller*, 1991; *Parker*, 1994; *Aster and Thurber*, 2013]. Alternatively, the penalized negative log likelihood can be interpreted in a fully Bayesian framework [*Akaike*, 1980] with a smooth prior distribution for $\boldsymbol{\mu}$, and γ can be chosen by maximizing the posterior probability of the model parameters $\boldsymbol{\theta}$, given the observed data (t_i, M_i) [*Tarantola*, 2005].

In our implementation of the regularized inversion algorithm, we minimize (3) using an iterative procedure. For a given data set, we first minimize the unpenalized negative log likelihood function (2) to obtain an initial guess at the mean background rate (μ) and the four other ETAS parameters ($\theta_{\text{ETAS}} = [K, \alpha, p, c\,]$). We then form an initial estimate for the time-varying background rate $\boldsymbol{\mu}$ by minimizing (3) with the four ETAS parameters held fixed. We then reestimate the θ_{ETAS} by minimizing (3), now with $\boldsymbol{\mu}$ held fixed. We repeat this procedure—alternately reestimating and fixing $\boldsymbol{\mu}$ and θ_{ETAS}, respectively—until convergence (i.e., negligible change in estimated parameter values by additional iteration). We adopt this iterative approach rather than minimize (3) directly in order to mitigate the effect of strong parameter tradeoffs between $\boldsymbol{\mu}$ and θ_{ETAS} [*Hainzl et al.*, 2013], which can bias numerical optimization algorithms. For the data sets used in this study, we find that the iterative algorithm converges rapidly (approximately three iterations).

2.4. Uncertainty Estimates for Model Parameters

The nonlinearity in the inversion process precludes a straightforward mapping between data and model uncertainties. We therefore use a form of Monte Carlo error propagation [*Ogilvie*, 1984] to compute uncertainty estimates in the model parameters. For a given set of earthquake catalog data, we first apply the methods described above to obtain a seismicity rate model for that data set. We then create an ensemble of 50 synthetic earthquake catalogs through stochastic simulation of an ETAS-like Poisson process [*Daley and Vere-Jones*, 2003] with the time-varying background rate function and ETAS parameters derived from the seismicity rate model. Finally, by treating each synthetic earthquake catalog as "data" and applying the seismicity rate inversion scheme described in the previous subsections, we obtain a distribution of seismicity rate models (i.e., one for each synthetic catalog) that approximate the uncertainty and covariance structure of the seismicity rate model of the true (i.e., observed) earthquake catalog data.

2.5. Testing for Changes in *b* Value and Magnitude Distribution

We use two distinct methods to examine temporal changes in the magnitude distributions of earthquakes within each geothermal field. For the first method, we assume that the cumulative magnitude distribution of

earthquakes in each field can be approximated by a Gutenberg-Richter distribution [*Gutenberg and Richter*, 1944] of the form $N \geq M = 10^{a-bM}$. We then compute the maximum likelihood estimate for the b value, b_{ml} [*Bender*, 1983; *Marzocchi and Sandri*, 2009]:

$$b_{\mathrm{ml}}(t_i) = \frac{1}{\log(10)\left[< M >_i - (M_c - \Delta M/2)\right]}, \tag{6}$$

at each earthquake occurrence time t_i by selecting all events with $M \geq M_c$ within a moving window of 401 total events, centered on event i. Here $< M >_i$ denotes the mean magnitude of all events within the window centered on event i, while ΔM denotes the magnitude increment within the earthquake catalog. This first approach has the advantage of being able to resolve the timing of significant changes in the first-order features of the magnitude distribution, but its efficacy depends strongly on the validity of the underlying assumption that the magnitude distribution does in fact follow a Gutenberg-Richter power law.

To mitigate this concern, our second method examines the full frequency-magnitude distributions of earthquakes within each field and allows for deviations from the standard power law at high magnitudes. For this method, we first divide the earthquake catalogs in each field into four 7 year, nonoverlapping time intervals. We then use a maximum likelihood technique to fit the magnitude distributions in each time interval with both standard Gutenberg-Richter (GR) and tapered Gutenberg-Richter model distributions [*Utsu*, 1999; *Kagan*, 2002]. The standard GR model is characterized by a single scalar parameter (the b value), while the tapered GR model is characterized both by a b value and upper corner magnitude M_x above which the magnitude distribution tapers to zero. We compare the fit of the two models to the observed earthquake data using an AIC test (equation (5)) that accounts both for the relative likelihood of the models and the difference in the number of free parameters (one for the standard GR model, and two for the tapered GR model). This second method is more powerful in resolving changes in the magnitude distribution at high magnitudes but lacks the finer temporal resolution of the first method (which uses a moving window approach).

3. Data and Resources

3.1. Earthquake Catalog Data

In this study, we use earthquake catalog data from two sources. For The Geysers, we use the waveform-relocated catalog of *Waldhauser and Schaff* [2008], which contains events in northern California from 1984 to 2011. For the Salton Sea and Coso geothermal fields, we use the waveform-relocated catalog of *Hauksson et al.* [2012], which contains events in southern California from 1981 to 2013. We first select all events within a rectangular box surrounding each geothermal field (Figure 1). We then estimate the minimum magnitude of completion M_c within each field for the years 1981–2013 (for Salton Sea and Coso) and 1984–2011 (for The Geysers) by applying the method of maximum curvature [*Woessner*, 2005] to 5 year, nonoverlapping windows of catalog data. Using this approach, we conservatively estimate that the catalog data for The Geysers, Salton Sea, and Coso are complete above magnitude 2.0, 2.0, and 1.5, respectively (Table 1), over their entire duration. As an additional test, we used a moving window approach to search for short-term transients in M_c. We found that M_c increases during swarms and other active earthquake sequences but does not exceed our cutoff values. While M_c for each field is typically lower than these thresholds in more recent years, we use the more conservative M_c values listed above to avoid introducing temporal biases into our seismicity analyses. Thus, we can interpret the seismicity rates we estimate as the rate of earthquakes of magnitude $M \geq M_c$ within the geothermal field boundary. We note here that the magnitudes from the Waldhouser-Schaff catalog for The Geysers are local magnitudes (M_L) as listed by the Northern California Seismic Network (NCSN) catalog, while the magnitudes from the Haukkson-Shearer relocated catalog for the Salton Sea and Coso are the Southern California Seismic Network (SCSN) preferred magnitudes. These are typically moment magnitude M_w when available, and local or helicorder magnitude otherwise.

In choosing to model seismicity only within the rectangular boundaries surrounding each geothermal field, we make the implicit assumption that aftershock triggering from earthquakes located outside each boundary has a relatively small impact on seismicity rates within the boundary itself. In cases where this assumption is violated, the inferred background seismicity rate will increase within the field [*Sornette*, 2005], so it is important to consider the influence of tectonic stresses from regional seismicity when interpreting transient increases in field-wide seismicity rates. As we will show below, regional seismicity near The Geysers is predominantly

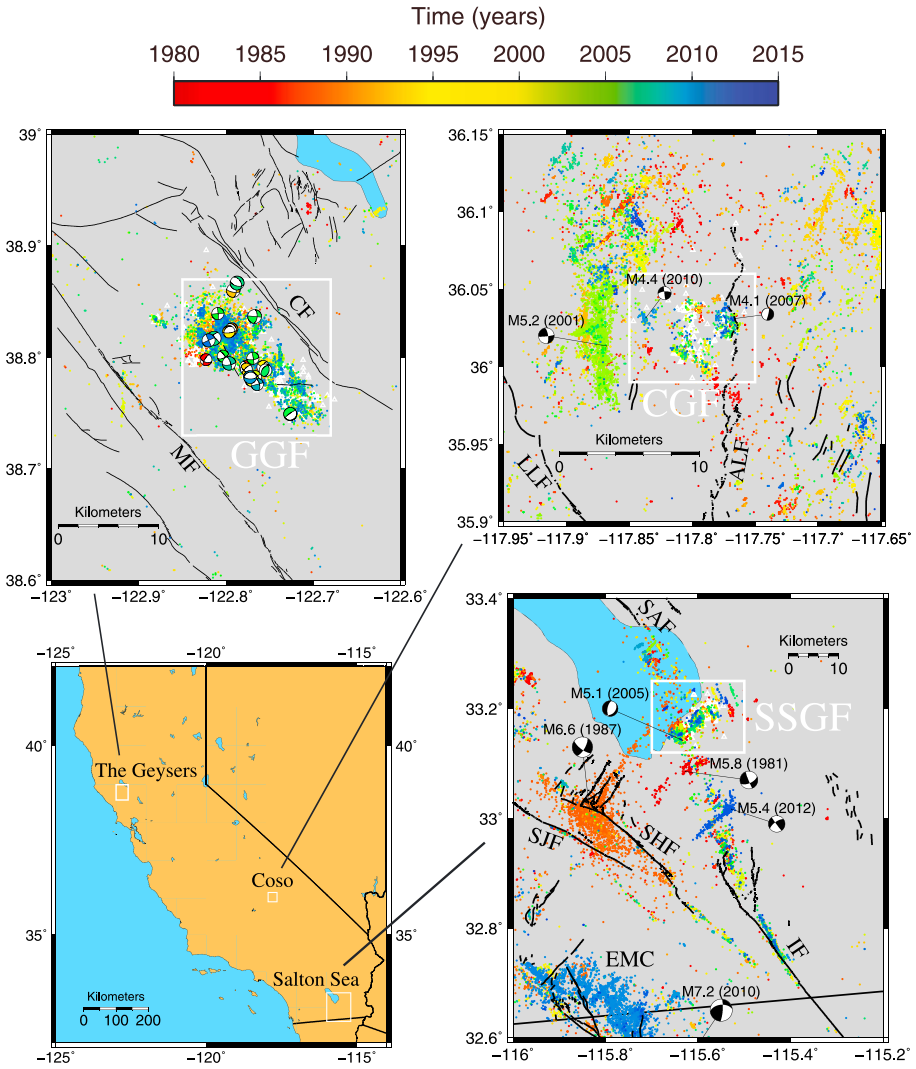

Figure 1. Map view of seismicity at The Geysers, Coso, and Salton Sea geothermal fields. Earthquake locations are from the catalogs of *Waldhauser and Schaff* [2008] and *Hauksson et al.* [2012], with each event color coded by its occurrence time (years). The study area boundaries for The Geysers (GGF), Coso (CGF), and Salton Sea (SSGF) geothermal fields are outlined in white, with well locations from the Department of Oil, Gas, and Geothermal Resources (DOGGR) database (http://www.conservation.ca.gov/dog/geothermal) denoted with white triangles. Quaternary faults (http://earthquake.usgs.gov/hazards/qfaults) are outlined in black. Focal mechanisms for $M \geq 4$ earthquakes within GGF are color coded by year.

composed of events within the geothermal field boundary, while there is evidence at both Salton Sea and Coso that regional seismicity influences local seismicity within the fields themselves.

3.2. Geothermal Operational Data

California state law requires geothermal fields within the state to release field-wide production (i.e., extracted fluid) volume and injection volume data to the California Department of Conservation's Department of Oil, Gas, and Geothermal Resources (DOGGR) on a monthly basis. We use the monthly production and injection data from the DOGGR online database (available at http://www.conservation.ca.gov/dog/geothermal) for comparison with our seismicity rate models. For The Geysers, production and injection data extend back to year 1969, well before the start of the northern California relocated earthquake catalog (1984). For the Salton Sea and Coso geothermal fields, production and injection data extend back to years 1982 and 1986, respectively, both of which are after the start of the southern California relocated earthquake catalog (1981). Production and injection data are available for each field through 2015, after the cessation of both relocated earthquake catalogs.

Table 1. Earthquake Catalog Data for The Geysers, Salton Sea, and Coso

Field Name	Catalog Duration (years)	Longitude Bounds (°E)	Latitude Bounds (°N)	M_c	N_{events}
The Geysers	1984–2011	[−122.85, −122.68]	[38.73, 38.87]	2.0	8857
Salton Sea	1981–2013	[−115.70, −115.50]	[32.12, 33.25]	2.0	1992
Coso	1981–2013	[−117.85, −117.75]	[35.99, 36.05]	1.5	1201

4. Results

4.1. The Geysers

4.1.1. Background

The Geysers, located approximately 120 km north of San Francisco (Figure 1), is California's largest geothermal field [*Geothermal Energy Association*, 2013; *Matek and Gawell*, 2014]. Producing an average of 666 MW of electric power in 2014 [*Calpine*, 2014; *Boyd et al.*, 2015], The Geysers generates enough energy to supply nearly 1 million residents in northern California. Energy production at The Geysers began in 1960s and peaked in 1987 [*Adams*, 2011], after which production declined during the 1990s due to fluid depletion within the geothermal reservoir. Initially, the only form of fluid injection to take place was the disposal of wastewater from steam production at the field itself [*Adams*, 2011]. In 1997, however, a pipeline was constructed to transport treated water from the Lake County Sanitation Plant for the purpose of fluid injection in the southeast sector of The Geysers [*Adams*, 2011; *Calpine*, 2014]. This new pipeline both removed excess wastewater from the Lake County sewage system (which was over capacity in the wet winter months) while simultaneously helping to replenish reservoir volumes at The Geysers through increased fluid injection. In 2003, a second pipeline to the northwest sector of The Geysers was created as part of the Santa Rosa Recharge Project [*Majer and Peterson*, 2007; *Vasco et al.*, 2013; *Martinez-Garzon et al.*, 2014], and the Santa Rosa pipeline now accounts for most of the injected wastewater volume at The Geysers [*Calpine*, 2014].

The geothermal reservoir at The Geysers is vapor dominated (i.e., gas is the dominant phase within the reservoir), rather than liquid dominated (as at Salton Sea and Coso), making The Geysers unique among California geothermal fields [*Matek and Gawell*, 2014]. Electric power is produced from hot steam that is extracted from wells within the reservoir at depths of 1–3 km [*Calpine*, 2014]. The 14 producing plants at The Geysers are concentrated within its northwest and southeast sectors. While the Northwest Geysers in particular has seen increased development in the years since the completion of the Santa Rosa pipeline [*Majer and Peterson*, 2007], total power production at The Geysers as a whole has declined since its peak in the late 1980s due to more concerted efforts to achieve a net fluid balance within the reservoir [*Boyd et al.*, 2015].

4.1.2. Changes in Background Seismicity Rate

It is well established that seismicity within The Geysers is modulated by geothermal plant operation [*Majer*, 1978; *Stark*, 1992; *Gomberg and Davis*, 1996; *Mossop and Segall*, 1999], and there was little historical seismicity in the region prior to the start of energy production in 1960 [*Oppenheimer*, 1986]. Previous studies have suggested that the total seismicity rate within the field has remained nearly constant since the 1980s, despite declining production volumes and changes to injection patterns [*Majer and Peterson*, 2007]. More recently, changes in injection patterns after the completion of the Santa Rosa pipeline have motivated a number of studies to investigate the effects of isolated injection events using microseismic [*Martinez-Garzon et al.*, 2014] and surface deformation [*Vasco et al.*, 2013] data. Here we apply the methodology developed in section 2 to analyze field-wide changes in seismicity from 1984 to 2011. Our seismicity rate model partitions the total seismicity rate $\lambda(t)$ into a time-varying background seismicity rate $\mu(t)$, and an interaction seismicity rate $\nu(t)$ that captures expected seismicity due to aftershock activity. The latter is parameterized in terms of a set of ETAS parameters $\theta_{\text{ETAS}} = [K, \alpha, p, c]$ that describe the intensity and temporal decay of typical aftershock sequences within the field.

The results of our seismicity rate inversion for The Geysers are summarized in Figure 2 and Table 2. The inferred background seismicity rate $\mu(t)$ in particular exhibits a number of interesting features. When averaged over timescales greater than a year or so, the background rate stays approximately constant at ~ 0.7 earthquakes/day from 1984 to 2003, which is consistent with the widely held notion of a steady seismicity rate at The Geysers since the 1980s [*Majer and Peterson*, 2007]. However, using our methodology we find that the background seismicity rate increases notably to an average of ~ 1.0 earthquakes/day after 2003, when injection volumes increased due to the installation of the Santa Rosa pipeline. Furthermore, we find that the

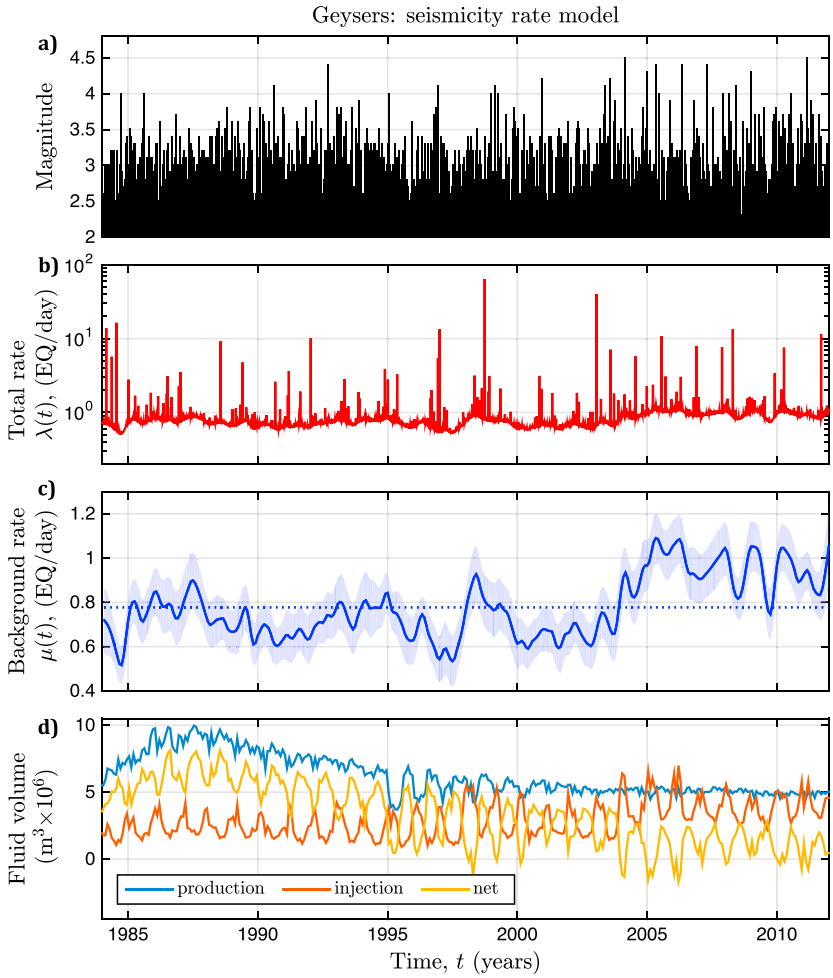

Figure 2. Seismicity rate model for The Geysers. (a) Magnitude versus time for earthquakes within the field. Magnitudes are of local type, as listed by the NCSN. (b) Total seismicity rate, $\lambda(t) = \mu(t) + \nu(t)$. (c) Background seismicity rate $\mu(t)$, with 2 sigma error bars (shaded) and mean rate (dotted line) plotted for reference. (d) Monthly rate of fluid production (blue), injection (red), and net production (production minus injection, yellow) at The Geysers (data available at http://www.conservation.ca.gov/dog/geothermal).

background rate exhibits seasonal oscillations, with peaks in seismicity that are aligned with peaks in the monthly fluid injection volumes of the field (Figure 2d). Fluid injection at The Geysers is itself highly seasonal [*Majer et al.*, 2007; *Adams*, 2011], with higher injection volumes during the winter months when more wastewater is available. Seismicity follows this same seasonal pattern, with higher background seismicity rates during the winter than during the summer. These seasonal peaks in seismicity are particularly pronounced in 1997–1998 (after the Lake County pipeline installation) and in the years since 2003 (after the Santa Rosa pipeline installation).

We quantify these observations more formally using stepwise linear regression analysis [*Mendenhall and Sincich*, 2007]. Applying this technique to The Geysers over the full catalog duration (1984–2011), we find that the correlation coefficient between monthly injection and background seismicity rate is 0.61, with a vanishingly small p value for the regression model (1.5×10^{-34}, a value which represents the inferred probability that the correlation could be zero, given the data). These statistical tests strongly corroborate the visual correlation apparent in Figure 2. Notice that while production rates at The Geysers followed the same seasonal pattern as injection during the 1980s and 1990s, in more recent years production has been nearly constant, with only injection following a seasonal pattern (Figure 2d). Seasonality in background seismicity rate becomes even more pronounced in these more recent years, indicating that stresses from injection, and not production, drive the observed seasonal patterns in seismicity at The Geysers.

Table 2. ETAS Parameter Estimates (and 95% Confidence Intervals)[a]

Field Name	K (95% CI)	α (95% CI)	p (95% CI)	c (days) (95% CI)	R_b (95% CI)
The Geysers	0.0005	0.77	1.56	0.0010	0.10
	(0.0002, 0.0011)	(0.71, 0.84)	(1.41, 1.77)	(0.0007, 0.0015)	(0.09, 0.11)
Salton Sea	0.026	0.41	1.21	0.0018	0.74
	(0.021, 0.028)	(0.37, 0.47)	(1.19, 1.27)	(0.0016, 0.0026)	(0.69, 0.79)
Coso	0.016	0.50	1.12	0.0008	0.48
	(0.011, 0.017)	(0.41, 0.56)	(1.10, 1.23)	(0.0005, 0.0017)	(0.42, 0.53)

[a]CI, confidence interval.

4.1.3. Changes in *b* Value, Magnitude Distribution, and Depth Distribution

Temporal changes in the magnitude and depth distributions of earthquakes can provide additional information about the evolution of stresses within The Geysers beyond that provided by analysis of seismicity rate changes alone. As a preliminary test for changes in magnitude distribution at The Geysers, we apply the first method detailed in section 2.5 to compute maximum likelihood *b* value estimates over 401-event moving windows. We observe an increase in *b* value beginning in late 2003 (Figure 3a), coinciding with the construction of the Santa Rosa pipeline. It is important to note, however, that this approach maps any potential change in the overall magnitude distribution into a change in a single scalar parameter, *b*. As such, if one looks only for changes in *b* value, one may miss more subtle changes in the magnitude distribution as a whole. Indeed, when we divide the 28 year catalog for The Geysers into four 7 year intervals and directly compare the magnitude distributions of each interval, the most obvious visual change is not a change in *b* value but rather a noticeable increase in large ($M \geq 3.5$) events in recent years (Figure 3b).

To quantify the significance of this observation, we use the second method described in section 2.5 to fit the full magnitude distributions in each time interval with both standard Gutenberg-Richter (GR) and tapered Gutenberg-Richter model distributions [*Utsu*, 1999; *Kagan*, 2002]. The standard GR model is characterized by one parameter: the *b* value, while the tapered GR model is characterized by two: the *b* value and a upper corner magnitude M_x above which the magnitude distribution tapers to zero. At The Geysers, we find that the *b* value is relatively constant during the first three time intervals but increases from 1.13 (2σ confidence interval of 1.08–1.18) during the third interval (1998–2004) to 1.26 (1.21–1.31) during the fourth interval (2005–2011). We also find that the corner magnitude of the tapered GR model increases with time, from 3.64 (3.50–3.78) during 1984–1991 to 4.63 (4.00–5.26) during 2005–2011. This latter estimate should be interpreted with some caution, however, as the tapered GR distribution provides a better model fit (lower AIC) only during

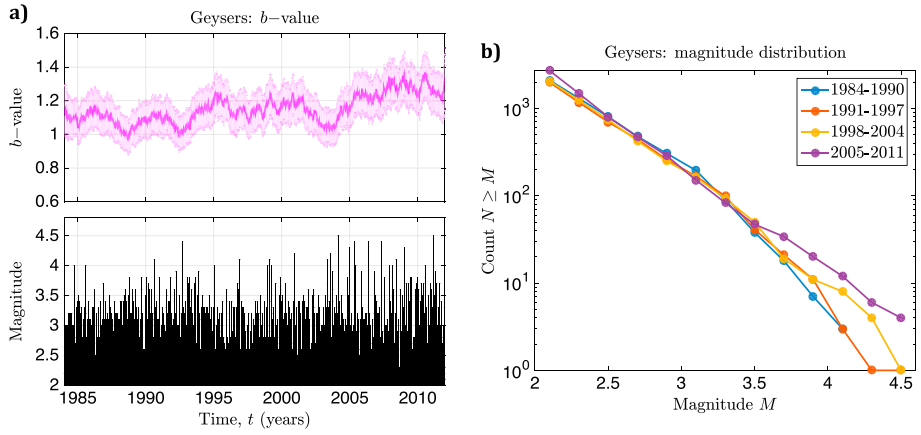

Figure 3. Magnitude distribution of earthquakes at The Geysers. (a, top) Maximum likelihood estimates for the Gutenberg-Richter *b* value (equation (6)) plotted as a function of time using a 401-event moving window. The 2 sigma error bars are shaded. (bottom) Magnitude versus time for earthquakes within the field, plotted for reference. Magnitudes are of local type, as listed by the NCSN. (b) Magnitude distributions for earthquakes at The Geysers during four, nonoverlapping time intervals (1984–1990, 1991–1997, 1998–2004, and 2005–2011).

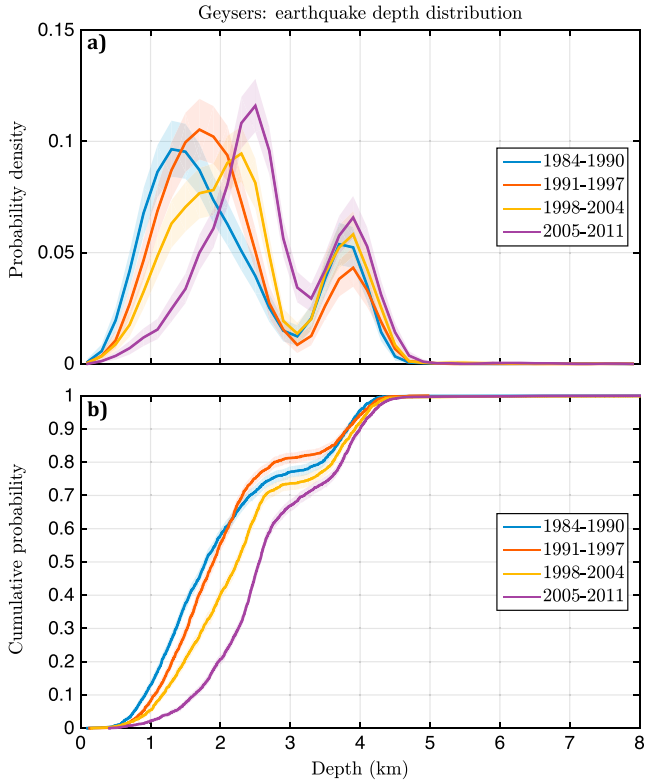

Figure 4. Depth distribution of earthquakes at The Geysers. (a) Probability density functions and (b) cumulative density functions for the depth distributions of earthquakes at The Geysers during the same four time intervals shown in Figure 3. Confidence intervals (95%) for the depth distributions are shaded.

the first three time intervals. Nevertheless, it appears that while the aforementioned increase in *b* value is significant, it is an incomplete description of the change in the magnitude distribution within The Geysers. Indeed, from a seismic hazard perspective, the increased frequency of large earthquakes in The Geysers is the more important temporal change to consider. We explore possible mechanisms responsible for these changes in section 5.

Like the magnitude distribution, the depth distribution of earthquakes at The Geysers also changes significantly with time. To show this, we divide the catalog into the same four equal time intervals as before and compare the probability density and cumulative density functions of earthquake depths during each interval (Figure 4). Since the error distribution for absolute hypocentral depth is not well constrained in the relocated earthquake catalogs and may evolve with time, we use a bootstrap technique [*Efron and Tibshirani*, 1994] to compute 95% confidence intervals for each depth distribution and analyze only the most robust features of the depth distributions. During all time intervals, the earthquake depth distribution at The Geysers is bimodal, with seismicity clustered around both shallower (1–3 km) and deeper (3–5 km) peaks in the depth distribution. The shallower peak corresponds to seismicity within and around the geothermal reservoir itself. The deeper cluster in seismicity consists almost exclusively of events within the Northwest Geysers. Previous studies [*Stark*, 2003] have suggested that these deeper events may correspond to earthquakes induced by thermoelastic stresses from injected fluid that has diffused from the geothermal reservoir (which is composed predominantly of greywacke rocks) into the metamorphosed, hornfelsic metagreywacke rocks in the high-temperature zone (HTZ) beneath the reservoir [*Jeanne et al.*, 2014; *Boyle and Zoback*, 2014].

While earthquakes at The Geysers exhibit this characteristic bimodal depth distribution during all time periods, the overall shape of the distribution (i.e., the location, width, and intensity of the peaks in the distribution) has evolved over time. Most notably, the shallow peak in seismicity has become both sharper and deeper with time (Figure 4), with the shallow peak shifting from its initial position of 1.45 $\pm$ 0.3 km depth (1984–1990) to 2.45$\pm$0.1 km depth in the most recent years (2005–2011). This transformation may be caused by changes in geothermal plant operation at The Geysers. In particular, the increase in injection volumes in the

Northwest Geysers from the Santa Rosa pipeline likely caused the shallower seismicity to cluster around the mean injection well depth of 2.5 km in that sector. Moreover, while the deeper cluster in seismicity (3–5 km) does not exhibit a shift in peak location with time, it is most prominent in these later years, when injection at the Northwest Geysers was at its most prevalent.

4.2. Salton Sea Geothermal Field

4.2.1. Background

The Salton Sea Geothermal Field (SSGF) is located in southeastern California, on the southern shore of the Salton Sea. The surrounding region, known as the Salton Trough, is tectonically active and encompasses the Pacific-North America plate boundary as it transitions from an extensional spreading center in the Gulf of California to a predominantly strike-slip boundary in central and northern California. The SSGF itself lies within the extensional stepover between the Imperial and Southern San Andreas Faults [*Muffler and White*, 1969; *Younker et al.*, 1982; *Crowell et al.*, 2013], with the San Jacinto and Superstition Hills Fault Zones located to the west of the SSGF (Figure 1). Earthquake swarms—spatially and temporally clustered earthquake sequences with no clear main shock—are relatively common occurrences in the region, with the 1981 Westmorland Swarm, 2005 Obsidian Buttes Swarm, and 2012 Brawley Swarm (each with multiple $M5+$ events) being the most notable examples [*Vidale and Shearer*, 2006; *Lohman and McGuire*, 2007; *Hauksson et al.*, 2013]. Regional fault systems also produce large earthquakes that follow more typical main shock-aftershock sequences, such as the 1987 $M6.6$ Superstition Hills [*Hudnut et al.*, 1989] and the 2010 $M7.2$ El Mayor-Cucapah [*Wei et al.*, 2011] earthquakes. The El Mayor-Cucapah event ruptured a set of faults within the Cucapah Mountains in Baja California [*Fletcher et al.*, 2014; *Gonzalez-Ortega et al.*, 2014], but its extensive aftershock sequence extended northward into the Salton Trough [*Hauksson et al.*, 2011].

The SSGF reservoir is liquid dominated, and the hot brine that exists in situ in the reservoir must therefore be flashed to steam to produce electricity. Energy production at the SSGF did not begin until the 1980s (more than 20 years after the initial development of The Geysers), in part due to the highly saline nature of the geothermal brine in the SSGF reservoir [*Adams*, 2011], which rapidly corroded much of the initial production well and pipeline infrastructure. Technological advances helped mitigate these early problems, making energy production more cost efficient and allowing for further development of the field. Construction of the geothermal plant was mostly complete by the early 1990s, though additional wells have been regularly constructed in the years since. The current energy production capacity of the SSGF is 437 MW [*Matek and Gawell*, 2014], but there is still significant potential for future growth [*Adams*, 2011], as the SSGF's vast geothermal reservoir is estimated to be capable of producing up to 1800 MW of power [*Matek and Gawell*, 2014]. However, the high upfront costs associated with energy production in the Salton Trough, along with the inherent difficulties of energy transport to more populous regions of California, may prevent further expansion of the SSGF.

4.2.2. Changes in Background Seismicity Rate

In Figure 5, we show the results of applying our method to compute seismicity rate changes (section 2) within the SSGF. We use the relocated earthquake catalog of *Hauksson et al.* [2012], which runs from 1981 to 2013 and thus contains events that occurred both before and during geothermal plant operation. We find that the background seismicity rate increases from a mean value of 0.01 earthquakes/day in 1981–1985, prior to geothermal plant operation, to a mean value of ~0.04 earthquakes/day in 1987, roughly a year after production began (Figure 5c). From year 1990 onward, the background seismicity rate remains relatively steady about this mean value, with occasional, but transient, increases or decreases in seismicity rate. These short-term fluctuations do not appear to be correlated with changes in operation at the SSGF field (Figure 5d). Instead, these fluctuations (such as the short-term rate increase observed in 2000–2001), seem more consistent with swarm-like earthquake sequences [*Lohman and McGuire*, 2007] driven by transient, but natural, tectonic stresses [*Llenos et al.*, 2009]. We discuss this hypothesis further in section 5.

We confirmed the apparent lack of correlation in the later years more formally by performing stepwise linear regression analysis [*Mendenhall and Sincich*, 2007]. In so doing, we found no evidence for any systematic relationship between background seismicity rate and any linear combination of monthly production or injection volumes at the SSGF in the years since 1990. Applying this same technique to the years preceding 1990, however, we find that the background seismicity rate is correlated with a linear model composed of both injection and net production (production minus injection) volumes, with a model correlation coefficient of 0.74 (and p value for the regression model of 1.27×10^{-18}). This correlation in these early years of plant operation

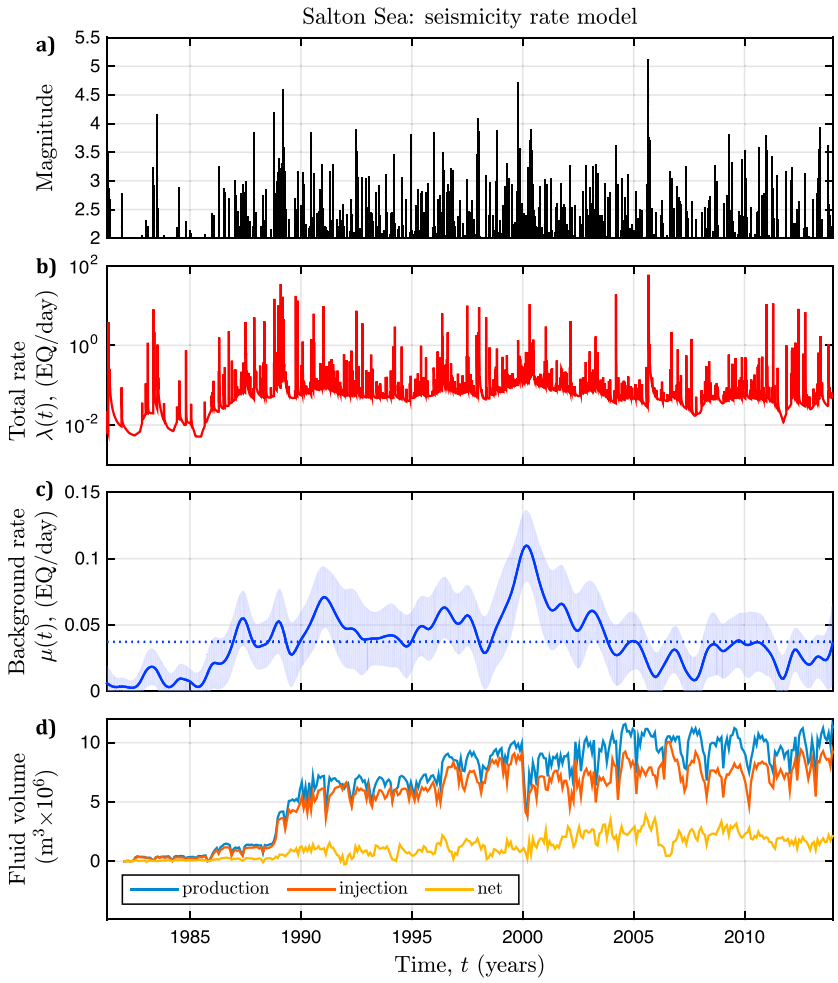

Figure 5. Seismicity rate model for Salton Sea. (a) Magnitude versus time for earthquakes within the field. Listed magnitudes are the SCSN preferred estimate. (b) Total seismicity rate, $\lambda(t) = \mu(t) + \nu(t)$. (c) Background seismicity rate $\mu(t)$, with 2 sigma error bars (shaded) and mean rate (dotted line) plotted for reference. (d) Monthly rate of fluid production (blue), injection (red), and net production (production minus injection, yellow) at Salton Sea (data available at http://www.conservation.ca.gov/dog/geothermal).

is consistent with our previous observation of a coincident rise in background rate and energy production during the late 1980s, but it is important to note that the relationship between the two may well be nonlinear.

Brodsky and Lajoie [2013] used a similar approach based on the ETAS model to compare temporal changes in seismicity rate to geothermal production and injection data from the SSGF. Although their methodology differs somewhat from ours, their background seismicity rate model also exhibits a robust rate increase that begins shortly after initial energy production at the Salton Sea. Moreover, *Brodsky and Lajoie* [2013] show that both net production and injection data, rather injection data alone, are necessary to explain changes in seismicity rate during this time. *Brodsky and Lajoie* [2013] also find that the relationship between seismicity rate and geothermal production and injection is less straightforward after 1990, although they proceed to construct a linear model of injection, net production, and seismicity rates by allowing for time variations in the regression coefficients. We do not attempt to recreate a complex model of this type here because of the inherent instabilities in fitting a large number of free parameters.

4.2.3. Changes in *b* Value, Magnitude Distribution, and Depth Distribution

We also find evidence for significant time variations in the magnitude and depth distributions of earthquakes within the SSGF. Using the approach detailed in section 2.5, we first test for temporal changes in *b* value by computing maximum likelihood estimates over 401-event moving windows. The *b* value appears to slowly increase after production ramps up in the late 1980s, before experiencing a sharp decline in 2000–2001 (Figure 6a). This decline in *b* value coincides with the earthquakes swarms that occur within the field

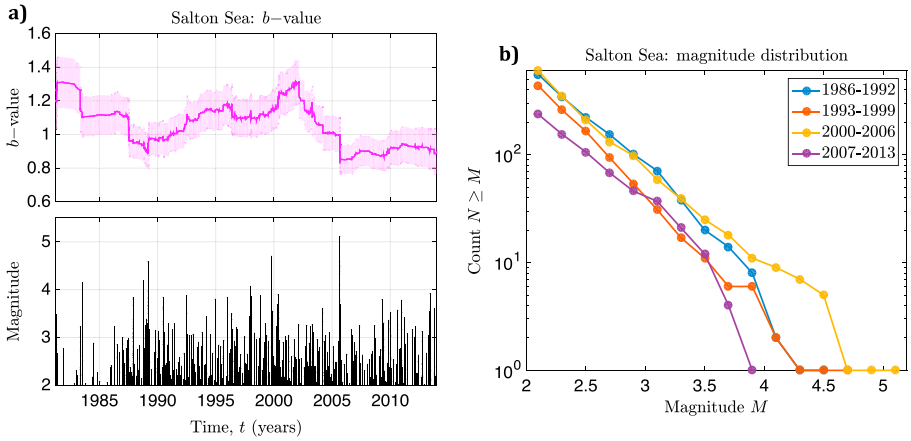

Figure 6. Magnitude distribution of earthquakes at Salton Sea. (a, top) Maximum likelihood estimates for the Gutenberg-Richter *b* value (equation (6)) plotted as a function of time using a 401-event moving window. Error bars (2 sigma) are shaded. (bottom) Magnitude versus time for earthquakes within the field, plotted for reference. Listed magnitudes are the SCSN-preferred estimate. (b) Magnitude distributions for earthquakes at Salton Sea during four, nonoverlapping time intervals (1986–1992, 1993–1999, 2000–2006, and 2007–2013).

during 2000 and 2001, with another sharp drop in *b* value occurring during the prominent 2005 Obsidian Buttes Swarm. The slow increase and subsequent sharp decrease in *b* value are also apparent when one examines the overall magnitude distributions for different time intervals (Figure 6b). In fitting both standard and tapered GR model distributions to each of the four intervals (section 4.1.3), we observe a decline in *b* value from 1.06 (2σ confidence interval of 0.97–1.14) during the third interval (2000–2006) to 0.91 (0.79–1.03) during the fourth (2007–2013). Interestingly, the standard GR model outperforms the tapered GR model (as measured by model AIC values) in all but the latest interval, which has an apparent corner magnitude M_x of 3.67 (3.42–3.92) that is significantly lower than any previous interval.

Changes in the depth distribution of earthquakes likewise suggest that both tectonic and anthropogenic stresses cause time-dependent changes in seismicity within the SSGF. In Figure 7, we compare earthquake depths in the SSGF over the same four time intervals. The depth distribution transitions from unimodal with a median value of 5.38 $\pm$ 0.13 km during the first interval (1986–1992), to bimodal, centered around that same depth, during the second interval (1993–1999). It is notable that the dominant fraction of these events occurs at depths greater than 4 km, which is far beneath typical reservoir depths of 1.0–2.5 km [*Younker et al.*, 1982]. During the third interval (2000–2006), the depth distribution includes a greater proportion of deep events (6–8 km) than in prior years, possibly a result of tectonic stresses associated with the 2000–2001 and 2005 swarms. During the final interval (2007–2013), however, the depth distribution both becomes notably shallower (median depth of 3.52 $\pm$ 0.15 km) and is strongly bimodal. These most recent years correspond to the highest levels of production and injection at the SSGF, and much of the seismicity is concentrated just beneath the reservoir.

4.3. Coso Geothermal Field

4.3.1. Background

Coso Geothermal Field (CGF) is located in eastern California, between the Southern Sierra Nevada and the Argus Range (Figure 1). This region is part of a broad transition zone between the strike-slip tectonics of the San Andreas Fault and the extensional tectonics of the Basin and Range province [*Duffield et al.*, 1980]. The CGF itself lies within an extensional step over between the Little Lake Fault to the southwest and a set of unnamed faults to the northeast, with the Airport Lake Fault striking northward through the field [*Monastero et al.*, 2005]. These faults, while active, accommodate only 6.5 mm/yr of dextral offset between the Argus Range and the Sierra Nevada [*McClusky et al.*, 2001]. Despite this relatively low tectonic deformation rate, the CGF and surrounding region are seismically active and, like the Salton Trough, prone to earthquake swarms [*Bhattacharyya and Lees*, 2002]. The most notable swarm in recent times occurred during the summer of 2001, culminating in a magnitude 5.2 earthquake just west of the geothermal field.

Coso Geothermal Field is California's third largest, with an installed capacity of 302 MW in 2014 and potential for more than 200 MW of expansion [*Matek and Gawell*, 2014]. A shallow magmatic chamber (5–8 km depth)

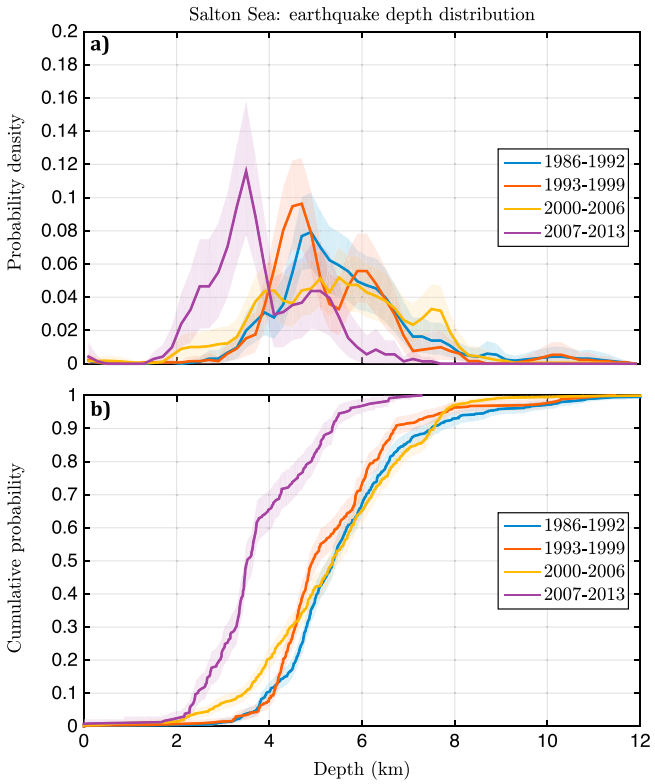

Figure 7. Depth distribution of earthquakes at Salton Sea. (a) Probability density functions and (b) cumulative density functions for the depth distributions of earthquakes at Salton Sea during the same four time intervals shown in Figure 6. Confidence intervals (95%) for the depth distributions are shaded.

acts as a heat source for the CGF's fluid-dominated geothermal reservoir, which ranges in depth from 0.5 to 3.5 km [*Duffield et al.*, 1980; *Manley*, 2000]. While privately owned, the CGF is located on the premises of the Naval Air Weapons Station at China Lake and is collaboratively managed by the Navy's Geothermal Program Office. Energy production at the CGF began in 1987 after a thorough review of the Coso area's potential as a geothermal resource [*Combs*, 1980], with further plant construction taking place until 1990 [*Monastero*, 2002]. Fluid production and injection volumes peaked in 1990 and have slowly declined in the years since, although technological improvements have allowed for consistent levels of energy production [*Matek and Gawell*, 2014]. Net fluid extraction at the CGF causes the surface to subside locally, creating poroelastic stresses within and near the reservoir [*Fialko and Simons*, 2000] and depleting the total fluid volume available for future energy production.

4.3.2. Changes in Background Seismicity Rate

Both tectonic and anthropogenic stresses are thought to contribute to observed seismicity at the CGF in the years since the plant's initial construction in 1987 [*Feng and Lees*, 1998; *Monastero et al.*, 2005; *Schoenball et al.*, 2015]. We use the relocated earthquake catalog of *Hauksson et al.* [2012] from 1981 to 2013 and the methods described in section 2 to construct a seismicity rate model for the CGF (Figure 8). As was observed at the Salton Sea Geothermal Field, the background seismicity rate within the CGF increases during the initial phase of energy production, with the background rate rising from a mean value of 0.02 earthquakes/day prior to 1987 to 0.05 earthquakes/day by 1990. After this time, the background seismicity rate fluctuates about this mean value, with short-term rate transients that do not appear to be modulated by geothermal injection or production (Figure 8d).

Application of a stepwise linear regression procedure [*Mendenhall and Sincich*, 2007] supports these observations. For 1987–1989, the optimal linear regression model obtained from this technique suggests that the background seismicity rate depends strongly on injection and production volumes during these years (correlation coefficient: 0.64, regression model p value: 2.9×10^{-6}). This result is consistent with our observation of a persistent increase in background rate starting during this time period. From 1990 on, however, the correlation is much weaker (correlation coefficient: 0.18), though not entirely insignificant, at least from

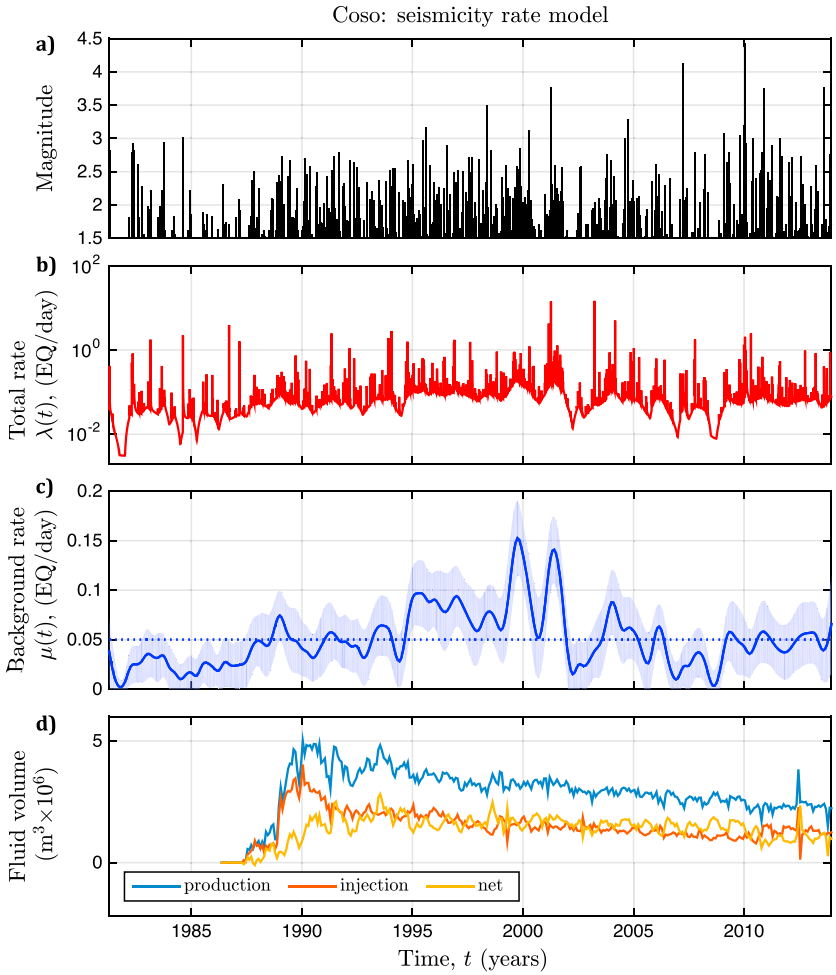

Figure 8. Seismicity rate model for Coso. (a) Magnitude versus time for earthquakes within the field. Listed magnitudes are the SCSN preferred estimate. (b) Total seismicity rate, $\lambda(t) = \mu(t) + \nu(t)$. (c) Background seismicity rate $\mu(t)$, with 2 sigma error bars (shaded) and mean rate (dotted line) plotted for reference. (d) Monthly rate of fluid production (blue), injection (red), and net production (production minus injection, yellow) at Coso (data available at http://www.conservation.ca.gov/dog/geothermal).

a statistical perspective (regression model p value = 1.7×10^{-3}). Note that because injection and production volumes track each other so closely at the CGF (Figure 8d), it is impossible to statistically distinguish whether one variable contributes more significantly than the other to potentially induced seismicity at the CGF.

While energy production does appear to have elevated the mean background seismicity rate at the CGF, the most prominent transient peaks in seismicity (e.g., during late 1994, 1999, and 2001) correspond to earthquake swarms and contain events both inside and far outside the field boundaries. The most prominent of these swarms took place during the summer of 2001, with a extended sequence of $M \geq 3$ earthquakes that occurred within and to the west of the CGF [*Hauksson and Unruh*, 2007]. The largest event in this swarm was a *M*5.2 earthquake that took place on 17 July 2001 and was located to the west of the field. The presence of these and other similar, far-reaching earthquake sequences are a reminder that the Coso area was seismically active long before the construction of the CGF [*Walter and Weaver*, 1980].

4.3.3. Changes in *b* Value, Magnitude Distribution, and Depth Distribution

The 2001 swarm also coincides with a fundamental change in the magnitude distribution of earthquakes within the CGF. Applying the moving window approach detailed in section 2.5, we find that the *b* value for earthquakes at the CGF has declined significantly since 2001 (Figure 9a). This change is also apparent in comparing the overall magnitude distributions of 7 year, nonoverlapping time intervals (Figure 9b). If we proceed as before and fit both standard and tapered GR model magnitude distributions to each of the four time intervals (section 4.1.3), the inferred *b* value of 0.79 (and 2σ confidence interval of 0.69–0.89) during 2007–2013

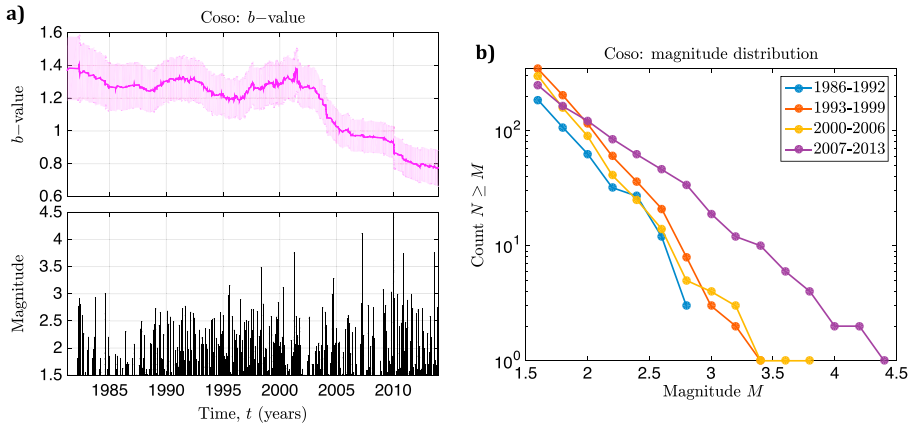

Figure 9. Magnitude distribution of earthquakes at Coso. (a, top) Maximum likelihood estimates for the Gutenberg-Richter *b* value (equation (6)) plotted as a function of time using a 401-event moving window. Error bars (2 sigma) are shaded. (bottom) Magnitude versus time for earthquakes within the field, plotted for reference. Listed magnitudes are the SCSN preferred estimate. (b) Magnitude distributions for earthquakes at Coso during four, nonoverlapping time intervals (1986–1992, 1993–1999, 2000–2006, and 2007–2013).

is much less than any of the previous intervals, which have *b* values in the range of 1.2–1.3. Further, during the most recent interval (2007–2013), larger earthquakes ($M \geq 3$) become more frequent both in relative and absolute terms, despite no appreciable change in seismicity rate since 1990. Both of the two recorded $M \geq 4$ earthquakes to occur within the field also took place during this time interval (a *M*4.1 event in 2007 and a *M*4.4 event in 2010) and are the only two $M \geq 4$ events to occur within the field boundary in the past 30 years [*Kaven et al.*, 2013]. These observations can also be quantified in terms of an increase in apparent upper corner magnitude M_x, which rises from 2.71 (2.41–3.00) during the first interval to 4.37 (3.71–5.04) during the final interval. We emphasize, however, that these corner magnitude estimates do not necessarily indicate a true deviation of the magnitude distribution from a standard Gutenberg-Richter power law, as AIC tests suggest that the data are actually better explained by the standard GR model (which has no corner magnitude) than the tapered GR model (which does).

The depth distribution of earthquakes within CGF also changes systematically with time. The median earthquake depth increases during each successive time interval (Figure 10), from a low of 1.09±0.10 km during the early years of energy production (1986–1992) to a high of 2.31±0.08 km during the final interval (2007–2013). This progressive shift in earthquake depth is puzzling and may in part be related to changes in production and injection volumes, both of which have been steadily declining since 1990 (Figure 8d). However, the deeper seismicity in recent years is composed predominantly of the earthquake sequences that are spatially clustered around the locations of the 2007 *M*4.1 and 2010 *M*4.4 events. Changes to the depth distribution may therefore reflect an altered stress state within the field in the aftermath of the 2001 swarm and the subsequent *M*4 events, though anthropogenic forcing may play a secondary role.

5. Discussion and Comparison of Geothermal Fields

5.1. Changes in Seismicity Rate

In the preceding section, we presented the results of our analysis of changes in background seismicity rates at The Geysers, Salton Sea, and Coso geothermal fields. The background seismicity rate at The Geysers is strongly correlated with fluid injection volume, and we observe significant rate increases associated with the installation of the Lake County and Santa Rosa pipelines. On shorter timescales, the seismicity rate exhibits a seasonal pattern that tracks the seasonality in available injection volumes. At the Salton Sea and Coso geothermal fields, the start of the earthquake catalog we use for our analyses predates initial plant operation, and we observe a significant increase in the background seismicity rate as operation commences. In later years, both the Salton Sea and Coso fields exhibit short-term fluctuations in background rate, as at The Geysers. However, in contrast to The Geysers, these fluctuations at Salton Sea and Coso are not strongly correlated with any discernible feature in monthly fluid injection or production volumes. We explore possible explanations for these differences below.

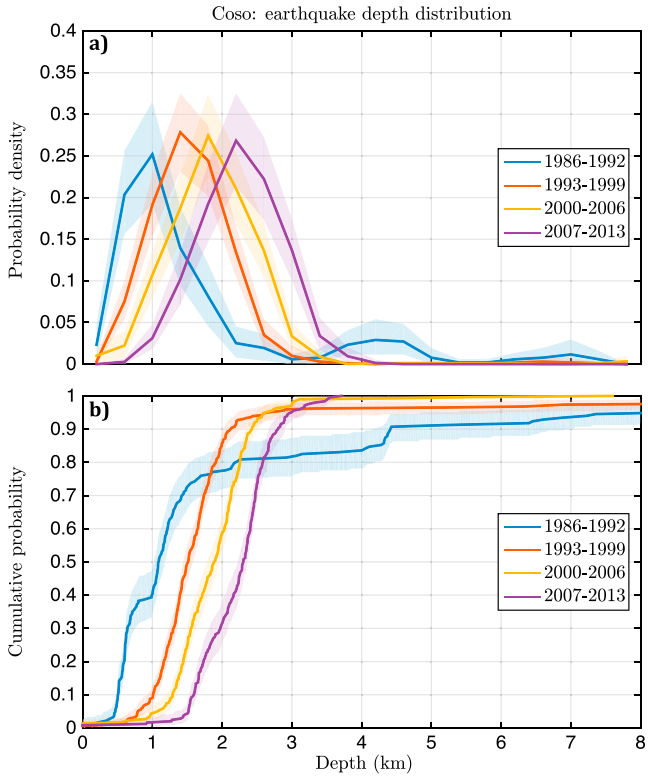

Figure 10. Depth distribution of earthquakes at Coso. (a) Probability density functions and (b) cumulative density functions for the depth distributions of earthquakes at Coso during the same four time intervals shown in Figure 9. Confidence intervals (95%) for the depth distributions are shaded.

Analyses of focal mechanisms [*Oppenheimer*, 1986; *Boyle and Zoback*, 2014] indicate that earthquakes within The Geysers occur on preexisting structures that are well aligned with the regional stress field. This suggests that regional tectonic stresses help supply much of the necessary background stress (as well as the in situ fault structures) for earthquakes to occur within The Geysers. However, as noted by *Oppenheimer* [1986] and others, there was little seismicity in and around The Geysers prior to the operation of the geothermal field. The intense cyclical pattern of fluid injection at The Geysers (which can exceed production during the winter months) may therefore provide the necessary stress perturbation to directly induce shear slip on faults that are near critically stressed by regional tectonics. Further, the extensive and transient fluid injection volumes, when combined with high in situ reservoir temperatures [*Stark*, 2003; *Jeanne et al.*, 2014] create localized thermoelastic stresses that greatly exceed tectonic stresses [*Altmann et al.*, 2013]. Indeed, *Martinez-Garzon et al.* [2013] observed a local temporal correlation between stress tensor orientation and injection rate for clusters of seismicity around selected injection wells in the northwest sector of The Geysers. Our results further demonstrate that at The Geysers, these transient anthropogenic stresses can plausibly modulate seismicity, even on a field-wide basis.

Nearly all of the seismicity in the region surrounding The Geysers is concentrated within the field itself (Figure 1). There is little observational evidence therefore that tectonic stress transients could account for the observed temporal changes in seismicity at The Geysers, though regional tectonic stresses undoubted contribute to slow, steady state loading of the in situ fault structures. In contrast, both Salton Sea and Coso are located in dynamic tectonic regions with active fault systems that surround the geothermal fields [*Younker et al.*, 1982; *Walter and Weaver*, 1980]. As a result, seismicity within the two geothermal fields is strongly influenced by natural processes of time-dependent tectonic stress transfer from regional earthquake activity, including the aseismic stress transients associated with the earthquake swarms characteristic of the Salton Trough and Coso Range. The elevated background seismicity rates observed at the Salton Sea (e.g., during 2000–2001) and Coso (e.g., during 1999 and 2001) correspond to earthquake swarms that are regional in scale

and extend well beyond the boundaries of the geothermal field. These fluctuations in seismicity rate due to natural (tectonic) stress transients tend to mask subtle changes in seismicity rate caused by anthropogenic stresses, especially since fluid injection and production volumes have remained relatively stable at both fields since their initial construction (unlike at The Geysers).

While our study has focused primarily on the background seismicity rate, it is also instructive to compare the set of inferred ETAS parameters (Table 2) that describe typical aftershock activity within each field. The Geysers in particular is notable for its anomalously low aftershock productivity parameter K, indicating that most earthquakes within The Geysers do not appear to trigger extensive aftershock sequences. We can formalize this observation by computing the branching ratio R_b, defined as the ratio of the expected number of triggered events (aftershocks) to total events, for each field. The inferred branching ratio of 0.09–0.11 at the Geysers is well below the 95% confidence interval for typical California seismicity [*Field et al.*, 2013]. The low aftershock productivity may indicate that most earthquakes at The Geysers are directly triggered by highly localized, anthropogenic stresses, rather than the more broadly distributed coseismic stresses from other earthquakes within the field. It has also been noted previously that earthquakes in northern California tend to have lower aftershock productivity than earthquakes in southern California [*Llenos*, 2014; *Brocher et al.*, 2015], so the very low aftershock productivity at The Geysers may be the consequence of both regional and local (i.e., energy production-related) factors. The inferred aftershock productivity (and hence, branching ratio) is higher at both the Salton Sea ($R_b = 0.69–0.79$) and Coso ($R_b = 0.42–0.52$) and is more typical of California seismicity. Both the Salton Sea and Coso have low inferred ETAS α parameters, as is common in regions prone to earthquake swarms [*Hainzl*, 2002; *Kumazawa et al.*, 2010; *Hainzl et al.*, 2013].

5.2. Changes in *b* Value, Magnitude Distribution, and Depth Distribution

At The Geysers, we observed a fundamental change in the earthquake magnitude distribution that coincided with the installation of the Santa Rosa pipeline in 2003. The significant increase in b value at this time is consistent with observational [*Shapiro et al.*, 2011; *Bachmann et al.*, 2011] and theoretical [*Bachmann et al.*, 2012; *Segall and Lu*, 2015] studies that suggest that induced earthquakes tend to have higher b values than natural earthquakes. However, the change in the magnitude distribution is more subtle than a simple change in b value, as the rate of large ($M \geq 4$) earthquakes also increases during this time. This latter phenomenon may be explained in part by the increased concentration of events in the deeper northwest sector of The Geysers after 2003, which appears to be characterized by a different magnitude distribution than the southeast sector [*Convertito et al.*, 2012]. *Kwiatek et al.* [2015] observed no significant variation in b value from 2007 to 2014 within certain clusters of seismicity within the northwest sector of The Geysers, which suggests that any field-wide changes in b value that may occur during these years are primarily due to an increased frequency of events occurring in the northwest sector, relative to the southeast sector, rather than changes within the northwest sector itself. We note, however, that most of the observed field-wide increase in b value occurs from 2003 to 2006 (Figure 3a), prior to the study of *Kwiatek et al.* [2015]. In addition to these longer-term trends, there is some evidence (Figure 3a) that the b value of earthquakes at The Geysers evolves on shorter timescales (perhaps even seasonally), a topic examined in more detail by *Convertito et al.* [2012] and *Martinez-Garzon et al.* [2014].

Earthquakes at the Salton Sea Geothermal Field, in contrast, appear to exhibit a slow increase in b value before year 2000, followed by steep declines in b value following earthquake swarms in 2000–2001 and 2005. Although the initial increase in b value following the beginning of energy production is consistent with previous studies of induced seismicity within geothermal fields [*Bachmann et al.*, 2011], the subsequent decline coincident with earthquake swarm activity suggests that natural tectonic processes (like those underlying swarm activity) strongly influence seismicity at the SSGF. Indeed, one would expect just such a decrease in b value during the earthquake swarms that characterize the Salton Trough, which tend to consist of multiple large earthquakes (with no clear main shock) and a relative deficiency of smaller earthquakes [*Lohman and McGuire*, 2007; *Chen and Shearer*, 2011].

Similarly, at Coso Geothermal Field, the b value remained relatively steady until 2001, when a prominent earthquake swarm occurred within and surrounding the field. The 2001 swarm included a $M5.2$ earthquake located to the west of the field, as well as a number of other $M \geq 3$ events both within and around the field. The apparent change in the magnitude distribution following this sequence is striking (Figures 9) and suggests that the swarm fundamentally altered the local stress state. It is notable that the largest earthquakes to occur within the field (including the only two $M \geq 4$ events) occurred either during or after the 2001 sequence.

Temporal changes to the depth distribution of earthquakes must be treated with some caution, as absolute errors in the hypocentral depths of the smaller earthquakes can be substantial. Nevertheless, while the overall depth distributions of each field are likely controlled by local geology and tectonics, the more robust features of the temporal changes in the depth distribution may reflect many of the same physical processes that control temporal changes in seismicity rates or magnitude distributions. For example, the deepening of the shallow peak of the bimodal distribution that characterizes The Geysers (Figure 4) is likely related to the increased concentration of events in the deeper northwest sector of The Geysers following the construction of Santa Rosa pipeline. The changes to the depth distributions at Salton Sea and Coso geothermal fields are more complex and undoubtedly modulated by both tectonic and anthropogenic stresses.

6. Concluding Remarks

The results we have presented here for The Geysers, Salton Sea, and Coso geothermal fields are concerned with long-term and field-wide changes in seismicity. It is well established that individual episodes of fluid injection or production can trigger microseismicity over short spatial and temporal scales [*Ellsworth*, 2013]. Here our central focus is not microseismicity, but rather the changing patterns of seismicity that can be observed over larger spatial scales (tens of kilometers) and longer time periods (months to decades). In seeking the smoothest model of background seismicity rate that adequately explains the observed earthquake catalog, our method is tailored to study robust changes in seismicity that occur over these same spatial and temporal scales. While we lack the resolution to explore highly transient or spatially isolated changes in seismicity, a uniform application of our methodology allows us to quantitatively compare temporal changes in seismicity at each geothermal field. In so doing, we can better assess the range of plausible mechanisms that may account for the differing responses of each field to tectonic and anthropogenic stressing.

At The Geysers, field-wide seismicity appears to be strongly controlled by anthropogenic stressing due to fluid injection and production. The mean background seismicity rate at The Geysers increased by 50% following the construction of the Santa Rosa pipeline in 2003 (and the associated increase in injection volume). Likewise, background seismicity rate increased after the installation of the Lake County pipeline in 1997, though this rate increase decayed with time as injection volumes returned to pre-1997 levels. Seasonal injection patterns at The Geysers — a consequence of more available fluid volume during the winter months — result in seasonal fluctuations in seismicity rate, which have become more intense in the years since the installation of the Santa Rosa pipeline. Fluid injection patterns also seem to influence the *b* value, magnitude distribution, and depth distribution of earthquakes within The Geysers, all of which show significant temporal changes that coincide with installation of the Santa Rosa pipeline.

The relationship between observed seismicity and geothermal energy production is less straightforward at the Salton Sea and Coso geothermal fields. At both the Salton Sea and Coso, the mean background seismicity rate increases during the initial phase of geothermal energy production, indicating anthropogenic stresses have an observable influence on field-wide seismicity. However, the most notable rate increases at both the Salton Sea and Coso are related to earthquake swarms that are regional in scale and extend far beyond the boundaries of the geothermal fields themselves. Earthquake swarms were prevalent in the Salton Sea and Coso regions before energy production began [*Lohman and McGuire*, 2007; *Bhattacharyya and Lees*, 2002], which suggests that the current swarms, which are not temporally correlated with changes to fluid injection or production, are caused by natural, rather than anthropogenic, stress transients. In any case, the presence of these swarms influences not only the seismicity rate but also the inferred *b* values, magnitude distributions, and depth distributions of earthquakes at both the Salton Sea and Coso geothermal fields.

Viewed holistically, our observations indicate that anthropogenic stresses are the primary control on transient changes in seismicity at The Geysers, while they play a less prominent role in modulating seismicity at Salton Sea and Coso. This is not to suggest that induced seismicity is of negligible concern at Salton Sea and Coso. Indeed, the proximity of the Salton Sea and Coso geothermal fields to active faults that are capable of producing large, damaging earthquakes amplifies the importance of even small changes in seismicity due to anthropogenic stresses [*Convertito et al.*, 2012; *Brodsky and Lajoie*, 2013]. Rather, these observations highlight the complicated process of differentiating induced from natural seismicity in California's geothermal fields, and demonstrate that differences in tectonic setting, reservoir conditions, and history of energy production all likely contribute to the differing patterns of seismicity observed within each geothermal field.

Acknowledgments
The relocated earthquake catalog for northern California (including The Geysers) is available from the NCEDC website (http://www.ncedc.org/ncedc/catalog-search.html), while the relocated earthquake catalog for southern California (including the Salton Sea and Coso) is available from the SCEDC website (http://scedc.caltech.edu/research-tools/alt-2011-dd-hauksson-yang-shearer.html). Fluid projection and injection data for The Geysers, Salton Sea, and Coso are available from the California Department of Conservation DOGGR website (http://www.conservation.ca.gov/dog/geothermal). This material is based upon work supported by the National Science Foundation Graduate Research Fellowship Program (NSFGRFP) under grant DGE-1144086. Additional support was provided by the Southern California Earthquake (SCEC) grant 14073. Map-based figures for this work were generated using the Generic Mapping Toolbox (GMT) [*Wessel et al.*, 2013]. We thank the Associate Editor and reviewers for their insightful comments, which greatly improved the manuscript, both in content and clarity. We also thank W. Wang, W. Neely, and Q. Zhang for illuminating internal discussions regarding early versions of this work.

References

Adams, J. W., (2011), The Geysers and Salton Sea Geothermal Fields, *Tech. Rep.*, California State Lands Commision - Mineral Resources Management Division, Long Beach, Calif.

Akaike, H. (1974), A new look at the statistical model identification, *IEEE Trans. Autom. Control*, *19*(6), 716–723, doi:10.1109/TAC.1974.1100705.

Akaike, H. (1980), Likelihood and the Bayes procedure, *Trabajos de Estadistica Y de Investigacion Operativa*, *31*(1), 143–166, doi:10.1007/BF02888350.

Ake, J., K. Mahrer, D. O'Connell, and L. Block (2005), Deep-injection and closely monitored induced seismicity at Paradox Valley, Colorado, *Bull. Seismol. Soc. Am.*, *95*(2), 664–683, doi:10.1785/0120040072.

Altmann, J. B., O. Heidbach, and R. Gritto (2013), Relative importance of processes leading to stress changes in The Geysers geothermal area, paper presented at 38th Workshop on Geothermal Reservoir Engineering, Stanford Univ., Stanford, Calif.

Aster, R. C., and C. H. Thurber (2013), *Parameter Estimation and Inverse Problems*, 2nd ed., Academic Press, Waltham, Mass.

Bachmann, C. E., S. Wiemer, J. Woessner, and S. Hainzl (2011), Statistical analysis of the induced Basel 2006 earthquake sequence: Introducing a probability-based monitoring approach for Enhanced Geothermal Systems: Probability-based monitoring approach for EGS, *Geophys. J. Int.*, *186*(2), 793–807, doi:10.1111/j.1365-246X.2011.05068.x.

Bachmann, C. E., S. Wiemer, B. P. Goertz-Allmann, and J. Woessner (2012), Influence of pore-pressure on the event-size distribution of induced earthquakes, *Geophys. Res. Lett.*, *39*, L09302, doi:10.1029/2012GL051480.

Bender, B. (1983), Maximum likelihood estimation of b values for magnitude grouped data, *Bull. Seismol. Soc. Am.*, *73*(3), 831–851.

Bhattacharyya, J., and J. M. Lees (2002), Seismicity and seismic stress in the Coso Range, Coso Geothermal Field, and Indian Wells Valley region, southeast-central California, in *Geologic Evolution of the Mojave Desert and Southwestern Basin and Range, Geol. Soc. Am. Mem.*, vol. 195, edited by A. F. Glazner, J. D. Walker, and J. M. Bartley, pp. 243–257, Geol. Soc. Am., Boulder, Colo.

Biot, M. A. (1941), General theory of three-dimensional consolidation, *J. Appl. Phys.*, *12*(2), 155–164, doi:10.1063/1.1712886.

Boyd, T. L., A. Sifford, and J. W. Lund (2015), The United States of America Country Update 2015, paper presented at World Geothermal Congress 2015, Melbourne, Australia.

Boyle, K., and M. Zoback (2014), The stress state of the Northwest Geysers, California Geothermal Field, and implications for fault-controlled fluid flow, *Bull. Seismol. Soc. Am.*, *104*(5), 2303–2312, doi:10.1785/0120130284.

Brocher, T. M., et al. (2015), The *Mw* 6.0 24 August 2014 South Napa Earthquake, *Seismol. Res. Lett.*, *86*(2A), 309–326, doi:10.1785/0220150004.

Brodsky, E. E., and L. J. Lajoie (2013), Anthropogenic seismicity rates and operational parameters at the Salton Sea Geothermal Field, *Science*, *341*(6145), 543–546, doi:10.1126/science.1239213.

Calpine (2014), The Geysers Geothermal Field 2014 statistics, *Tech. Rep.*, Calpine Corp., Middletown, Calif.

Chen, X., and P. M. Shearer (2011), Comprehensive analysis of earthquake source spectra and swarms in the Salton Trough, California, *J. Geophys. Res.*, *116*, B09309, doi:10.1029/2011JB008263.

Combs, J. (1980), Heat flow in the Coso geothermal area, Inyo County, California, *J. Geophys. Res.*, *85*(B5), 2411–2424, doi:10.1029/JB085iB05p02411.

Convertito, V., N. Maercklin, N. Sharma, and A. Zollo (2012), From induced seismicity to direct time-dependent seismic hazard, *Bull. Seismol. Soc. Am.*, *102*(6), 2563–2573, doi:10.1785/0120120036.

Crowell, B. W., Y. Bock, D. T. Sandwell, and Y. Fialko (2013), Geodetic investigation into the deformation of the Salton Trough, *J. Geophys. Res. Solid Earth*, *118*, 5030–5039, doi:10.1002/jgrb.50347.

Daley, D. J., and D. Vere-Jones (2003), *An Introduction to the Theory of Point Processes*, 2nd ed., Springer, New York.

Deichmann, N., and D. Giardini (2009), Earthquakes induced by the stimulation of an enhanced geothermal system below Basel (Switzerland), *Seismol. Res. Lett.*, *80*(5), 784–798, doi:10.1785/gssrl.80.5.784.

Duffield, W. A., C. R. Bacon, and G. B. Dalrymple (1980), Late Cenozoic volcanism, geochronology, and structure of the Coso Range, Inyo County, California, *J. Geophys. Res.*, *85*(B5), 2381–2404, doi:10.1029/JB085iB05p02381.

Efron, B., and R. J. Tibshirani (1994), *An Introduction to the Bootstrap*, CRC Press, Boca Raton, Fla.

Ellsworth, W. L. (2013), Injection-induced earthquakes, *Science*, *341*(6142), 1225942, doi:10.1126/science.1225942.

Feng, Q., and J. M. Lees (1998), Microseismicity, stress, and fracture in the Coso Geothermal Field, California, *Tectonophysics*, *289*(1–3), 221–238, doi:10.1016/S0040-1951(97)00317-X.

Fialko, Y., and M. Simons (2000), Deformation and seismicity in the Coso geothermal area, Inyo County, California: Observations and modeling using satellite radar interferometry, *J. Geophys. Res.*, *105*(B9), 21,781–21,793, doi:10.1029/2000JB900169.

Field, E. H., et al. (2013), Uniform California earthquake rupture forecast, version 3 (UCERF3)—The time-independent model, *U.S. Geol. Surv. Open File Rep. 2013–1165*, 97 p., California Geological Survey Special Report 228, and Southern California Earthquake Center Publication 1792. [Available at http://pubs.usgs.gov/of/2013/1165/.]

Fletcher, J. M., et al. (2014), Assembly of a large earthquake from a complex fault system: Surface rupture kinematics of the 4 April 2010 El Mayor-Cucapah (Mexico) M_w 7.2 earthquake, *Geosphere*, *10*(4), 797–827, doi:10.1130/GES00933.1.

Frohlich, C., and M. Brunt (2013), Two-year survey of earthquakes and injection/production wells in the Eagle Ford Shale, Texas, prior to the October 2011 earthquake, *Earth Planet. Sci. Lett.*, *379*, 56–63, doi:10.1016/j.epsl.2013.07.025.

Frohlich, C., C. Hayward, B. Stump, and E. Potter (2011), The Dallas-Fort worth earthquake sequence: October 2008 through May 2009, *Bull. Seismol. Soc. Am.*, *101*(1), 327–340, doi:10.1785/0120100131.

Geothermal Energy Association (2013), 2013 Annual U.S. geothermal power production and development report, *Tech. Rep.*, Geotherm. Energy Assoc., Washington, D. C.

Goebel, T. (2015), A comparison of seismicity rates and fluid-injection operations in Oklahoma and California: Implications for crustal stresses, *Leading Edge*, *34*(6), 640–648, doi:10.1190/tle34060640.1.

Gomberg, J., and S. Davis (1996), Stress/strain changes and triggered seismicity at The Geysers, California, *J. Geophys. Res.*, *101*(B1), 733–749, doi:10.1029/95JB03250.

Gonzalez-Ortega, A., Y. Fialko, D. Sandwell, F. Alejandro Nava-Pichardo, J. Fletcher, J. Gonzalez-Garcia, B. Lipovsky, M. Floyd, and G. Funning (2014), El Mayor-Cucapah (M_w 7.2) earthquake: Early near-field postseismic deformation from InSAR and GPS observations, *J. Geophys. Res. Solid Earth*, *119*, 1482–1497, doi:10.1002/2013JB010193.

Good, I. J., and R. A. Gaskins (1971), Nonparametric roughness penalties for probability densities, *Biometrika*, *58*(2), 255–277, doi:10.2307/2334515.

Gutenberg, B., and C. F. Richter (1944), Frequency of earthquakes in California, *Bull. Seismol. Soc. Am.*, *34*(4), 185–188.

Hainzl, S. (2002), Indications for a successively triggered rupture growth underlying the 2000 earthquake swarm in Vogtland/NW Bohemia, *J. Geophys. Res.*, *107*(B12), 2338, doi:10.1029/2002JB001865.

Hainzl, S., O. Zakharova, and D. Marsan (2013), Impact of aseismic transients on the estimation of aftershock productivity parameters, *Bull. Seismol. Soc. Am.*, *103*(3), 1723–1732, doi:10.1785/0120120247.

Hauksson, E., and J. Unruh (2007), Regional tectonics of the Coso geothermal area along the intracontinental plate boundary in central eastern California: Three-dimensional V_p and V_p/V_s models, spatial-temporal seismicity patterns, and seismogenic deformation, *J. Geophys. Res.*, *112*, B06309, doi:10.1029/2006JB004721.

Hauksson, E., J. Stock, K. Hutton, W. Yang, J. A. Vidal-Villegas, and H. Kanamori (2011), The 2010 M_w 7.2 El Mayor-Cucapah Earthquake Sequence, Baja California, Mexico and Southernmost California, USA: Active seismotectonics along the Mexican Pacific margin, *Pure Appl. Geophys.*, *168*(8–9), 1255–1277, doi:10.1007/s00024-010-0209-7.

Hauksson, E., W. Yang, and P. M. Shearer (2012), Waveform relocated earthquake catalog for southern California (1981 to June 2011), *Bull. Seismol. Soc. Am.*, *102*(5), 2239–2244, doi:10.1785/0120120010.

Hauksson, E., et al. (2013), Report on the August 2012 Brawley earthquake swarm in Imperial Valley, Southern California, *Seismol. Res. Lett.*, *84*(2), 177–189, doi:10.1785/0220120169.

Healy, J. H., W. W. Rubey, D. T. Griggs, and C. B. Raleigh (1968), The Denver earthquakes, *Science*, *161*(3848), 1301–1310.

Horton, S. (2012), Disposal of hydrofracking waste fluid by injection into subsurface aquifers triggers earthquake swarm in central Arkansas with potential for damaging earthquake, *Seismol. Res. Lett.*, *83*(2), 250–260, doi:10.1785/gssrl.83.2.250.

Hubbert, M. K., and W. W. Rubey (1959), Role of fluid pressure in mechanics of overthrust faulting, *Geol. Soc. Am. Bull.*, *70*(2), 115–166, doi:10.1130/0016-7606(1959)70[115:ROFPIM]2.0.CO;2.

Hudnut, K. W., L. Seeber, and J. Pacheco (1989), Cross-fault triggering in the November 1987 Superstition Hills Earthquake Sequence, southern California, *Geophys. Res. Lett.*, *16*(2), 199–202, doi:10.1029/GL016i002p00199.

Jeanne, P., J. Rutqvist, D. Vasco, J. Garcia, P. F. Dobson, M. Walters, C. Hartline, and A. Borgia (2014), A 3D hydrogeological and geomechanical model of an Enhanced Geothermal System at The Geysers, California, *Geothermics*, *51*, 240–252, doi:10.1016/j.geothermics.2014.01.013.

Kagan, Y. Y. (2002), Seismic moment distribution revisited: I. Statistical results, *Geophys. J. Int.*, *148*(3), 520–541, doi:10.1046/j.1365-246x.2002.01594.x.

Kaven, J. O., S. H. Hickman, and N. C. Davatzes (2013), *Micro-seismicity Within the Coso Geothermal Field, California, From 1996–2012*. paper presented at 38th Workshop on Geothermal Reservoir Engineering Stanford University, Stanford, Calif., 11–13 Feb.

Keranen, K. M., H. M. Savage, G. A. Abers, and E. S. Cochran (2013), Potentially induced earthquakes in Oklahoma, USA: Links between wastewater injection and the 2011 M_w 5.7 earthquake sequence, *Geology*, *41*(6), 699–702, doi:10.1130/G34045.1.

Keranen, K. M., M. Weingarten, G. A. Abers, B. A. Bekins, and S. Ge (2014), Sharp increase in central Oklahoma seismicity since 2008 induced by massive wastewater injection, *Science*, *345*(6195), 448–451, doi:10.1126/science.1255802.

Kim, W.-Y. (2013), Induced seismicity associated with fluid injection into a deep well in Youngstown, Ohio, *J. Geophys. Res. Solid Earth*, *118*, 3506–3518, doi:10.1002/jgrb.50247.

Kumazawa, T., and Y. Ogata (2013), Quantitative description of induced seismic activity before and after the 2011 Tohoku-Oki earthquake by nonstationary ETAS models, *J. Geophys. Res. Solid Earth*, *118*, 6165–6182, doi:10.1002/2013JB010259.

Kumazawa, T., Y. Ogata, and S. Toda (2010), Precursory seismic anomalies and transient crustal deformation prior to the 2008 M_w 6.9 Iwate-Miyagi Nairiku, Japan, earthquake, *J. Geophys. Res.*, *115*, B10312, doi:10.1029/2010JB007567.

Kwiatek, G., P. Martinez-Garzon, G. Dresen, M. Bohnhoff, H. Sone, and C. Hartline (2015), Effects of long-term fluid injection on induced seismicity parameters and maximum magnitude in northwestern part of The Geysers geothermal field, *J. Geophys. Res. Solid Earth*, *120*, 7085–7101, doi:10.1002/2015JB012362.

Llenos, A. L. (2014), The (Un)productivity of the 2014 *M*6.0 South Napa aftershock sequence, Abstracts S33F-4928 presented at 2014 Fall Meeting, AGU, San Francisco, Calif., 15–19 Dec.

Llenos, A. L., J. J. McGuire, and Y. Ogata (2009), Modeling seismic swarms triggered by aseismic transients, *Earth Planet. Sci. Lett.*, *281*(1–2), 59–69, doi:10.1016/j.epsl.2009.02.011.

Lohman, R. B., and J. J. McGuire (2007), Earthquake swarms driven by aseismic creep in the Salton Trough, California, *J. Geophys. Res.*, *112*, B04405, doi:10.1029/2006JB004596.

Majer, E. L. (1978), Seismological investigation in geothermal regions, PhD thesis, UC Berkeley, Berkeley, Calif.

Majer, E. L., and J. E. Peterson (2007), The impact of injection on seismicity at The Geysers, California Geothermal Field, *Int. J. Rock Mech. Min. Sci.*, *44*(8), 1079–1090, doi:10.1016/j.ijrmms.2007.07.023.

Majer, E. L., R. Baria, M. Stark, S. Oates, J. Bommer, B. Smith, and H. Asanuma (2007), Induced seismicity associated with Enhanced Geothermal Systems, *Geothermics*, *36*(3), 185–222, doi:10.1016/j.geothermics.2007.03.003.

Manley, C. R. (2000), Rhyolite thermobarometry and the shallowing of the magma reservoir, Coso Volcanic Field, California, *J. Petrol.*, *41*(1), 149–174, doi:10.1093/petrology/41.1.149.

Marsan, D., and O. Lengliné (2010), A new estimation of the decay of aftershock density with distance to the mainshock, *J. Geophys. Res.*, *115*, B09302, doi:10.1029/2009JB007119.

Marsan, D., E. Prono, and A. Helmstetter (2013), Monitoring aseismic forcing in fault zones using earthquake time series, *Bull. Seismol. Soc. Am.*, *103*(1), 169–179, doi:10.1785/0120110304.

Martinez-Garzon, P., M. Bohnhoff, G. Kwiatek, and G. Dresen (2013), Stress tensor changes related to fluid injection at The Geysers Geothermal Field, California, *Geophys. Res. Lett.*, *40*, 2596–2601, doi:10.1002/grl.50438.

Martinez-Garzon, P., G. Kwiatek, H. Sone, M. Bohnhoff, G. Dresen, and C. Hartline (2014), Spatiotemporal changes, faulting regimes, and source parameters of induced seismicity: A case study from The Geysers Geothermal Field: Characterization of induced seismicity, *J. Geophys. Res. Solid Earth*, *119*, 8378–8396, doi:10.1002/2014JB011385.

Marzocchi, W., and L. Sandri (2009), A review and new insights on the estimation of the *b*-value and its uncertainty, *Ann. Geophys.*, *46*(6), 1271–1282, doi:10.4401/ag-3472.

Matek, B., and K. Gawell (2014), Report on the state of geothermal energy in California, *Tech. Rep.*, Geotherm. Energy Assoc., Washington, D. C.

McClusky, S. C., S. C. Bjornstad, B. H. Hager, R. W. King, B. J. Meade, M. M. Miller, F. C. Monastero, and B. J. Souter (2001), Present day kinematics of the Eastern California Shear Zone from a geodetically constrained block model, *Geophys. Res. Lett.*, *28*(17), 3369–3372, doi:10.1029/2001GL013091.

Mendenhall, W., and T. Sincich (2007), *Statistics for Engineering and the Sciences*, Pearson Prentice-Hall, Upper Saddle River, N. J.

Monastero, F., A. Katzenstein, J. Miller, J. Unruh, M. Adams, and K. Richards-Dinger (2005), The Coso Geothermal Field: A nascent metamorphic core complex, *Geol. Soc. Am. Bull.*, *117*(11), 1534–1553, doi:10.1130/B25600.1.

Monastero, F. C. (2002), An overview of industry military cooperation in the development of power operations at the Coso Geothermal Field in southern California, *Geotherm. Res. Counc. Bull.*, *31*(5), 188–195.

Mossop, A., and P. Segall (1997), Subsidence at The Geysers Geothermal Field, N. California from a comparison of GPS and leveling surveys, *Geophys. Res. Lett.*, *24*(14), 1839–1842, doi:10.1029/97GL51792.
Mossop, A., and P. Segall (1999), Volume strain within The Geysers Geothermal Field, *J. Geophys. Res.*, *104*(B12), 29,113–29,131, doi:10.1029/1999JB900284.
Muffler, L. J., and D. E. White (1969), Active metamorphism of upper Cenozoic sediments in the Salton Sea Geothermal Field and the Salton Trough, Southeastern California, *Geol. Soc. Am. Bull.*, *80*(2), 157–182, doi:10.1130/0016-7606(1969)80[157:AMOUCS]2.0.CO;2.
National Resource Council (2013), *Induced Seismicity Potential in Energy Technologies*, Natl. Academic Press, Washington, D. C.
Nicholson, C., and R. L. Wesson (1992), Triggered earthquakes and deep well activities, *Pure Appl. Geophys.*, *139*(3–4), 561–578, doi:10.1007/BF00879951.
Ogata, Y. (1983), Estimation of the parameters in the modified Omori formula for aftershock frequencies by the maximum likelihood procedure, *J. Phys. Earth*, *31*(2), 115–124, doi:10.4294/jpe1952.31.115.
Ogata, Y. (1988), Statistical models for earthquake occurrences and residual analysis for point processes, *J. Am. Stat. Assoc.*, *83*(401), 9–27, doi:10.1080/01621459.1988.10478560.
Ogata, Y. (1992), Detection of precursory relative quiescence before great earthquakes through a statistical model, *J. Geophys. Res.*, *97*(B13), 19,845–19,871, doi:10.1029/92JB00708.
Ogata, Y. (2004), Space-time model for regional seismicity and detection of crustal stress changes, *J. Geophys. Res.*, *109*, B03308, doi:10.1029/2003JB002621.
Ogilvie, J. (1984), A Monte-Carlo approach to error propagation, *Comput. Chem.*, *8*(3), 205–207, doi:10.1016/0097-8485(84)80007-8.
Omori, F. (1894), Investigation of aftershocks, *Rep. Earthquake Invest. Commun.*, *2*, 103–139.
Oppenheimer, D. H. (1986), Extensional tectonics at The Geysers Geothermal Area, California, *J. Geophys. Res.*, *91*(B11), 11,463–11,476, doi:10.1029/JB091iB11p11463.
Parker, R. L. (1994), *Geophysical Inverse Theory*, Princeton Univ. Press, Princeton, N. J.
Press (Ed.), W. H. (2007), *Numerical Recipes: The Art of Scientific Computing*, 3rd ed., Cambridge Univ. Press, Cambridge, U. K., and New York.
Raleigh, C. B., J. H. Healy, and J. D. Bredehoeft (1976), An experiment in earthquake control at Rangely, Colorado, *Science*, *191*(4233), 1230–1237, doi:10.1126/science.191.4233.1230.
Rubinstein, J. L., W. L. Ellsworth, A. McGarr, and H. M. Benz (2014), The 2001-present induced earthquake sequence in the Raton Basin of Northern New Mexico and Southern Colorado, *Bull. Seismol. Soc. Am.*, *104*(5), 2162–2181, doi:10.1785/0120140009.
Schoenball, M., N. C. Davatzes, and J. M. G. Glen (2015), Differentiating induced and natural seismicity using space-time-magnitude statistics applied to the Coso Geothermal Field, *Geophys. Res. Lett.*, *42*, 6221–6228, doi:10.1002/2015GL064772.
Segall, P. (1989), Earthquakes triggered by fluid extraction, *Geology*, *17*(10), 942–946, doi:10.1130/0091-7613(1989)017<0942:ETBFE>2.3.CO;2.
Segall, P., and S. D. Fitzgerald (1998), A note on induced stress changes in hydrocarbon and geothermal reservoirs, *Tectonophysics*, *289*(1–3), 117–128, doi:10.1016/S0040-1951(97)00311-9.
Segall, P., and S. Lu (2015), Injection-induced seismicity: Poroelastic and earthquake nucleation effects, *J. Geophys. Res. Solid Earth*, *120*, 5082–5103, doi:10.1002/2015JB012060.
Segall, P., J.-R. Grasso, and A. Mossop (1994), Poroelastic stressing and induced seismicity near the Lacq gas field, southwestern France, *J. Geophys. Res.*, *99*(B8), 15,423–15,438, doi:10.1029/94JB00989.
Shapiro, S. A., O. S. Krüger, C. Dinske, and C. Langenbruch (2011), Magnitudes of induced earthquakes and geometric scales of fluid-stimulated rock volumes, *Geophysics*, *76*(6), WC55–WC63, doi:10.1190/geo2010-0349.1.
Snyder, D. L., and M. I. Miller (1991), *Random Point Processes in Time and Space*, Springer, New York.
Sornette, D. (2005), Apparent clustering and apparent background earthquakes biased by undetected seismicity, *J. Geophys. Res.*, *110*, B09303, doi:10.1029/2005JB003621.
Stark, M. (2003), Seismic evidence for a long-lived Enhanced Geothermal System (EGS) in The Northern Geysers reservoir, *Geotherm. Res. Counc. Trans.*, *27*, 727–731.
Stark, M. A. (1992), Microearthquakes: A tool to track injected water in The Geysers reservoir, in *Monograph on the Geysers Geothermal Field, Geotherm. Res. Counc. Special Rep. 17*, edited by C. Stone, pp. 111–117, Geothermal Resources Council, Davis, Calif.
Suckale, J. (2009), Induced seismicity in hydrocarbon fields, *Adv. Geophys.*, *51*, 55–106, Elsevier.
Tarantola, A. (2005), *Inverse Problem Theory and Methods for Model Parameter Estimation*, SIAM, Philadelphia, Pa.
Toda, S., R. S. Stein, and T. Sagiya (2002), Evidence from the AD 2000 Izu islands earthquake swarm that stressing rate governs seismicity, *Nature*, *419*(6902), 58–61, doi:10.1038/nature00997.
Trugman, D. T., A. A. Borsa, and D. T. Sandwell (2014), Did stresses from the Cerro Prieto Geothermal Field influence the El Mayor-Cucapah rupture sequence?, *Geophys. Res. Lett.*, *41*, 8767–8774, doi:10.1002/2014GL061959.
Utsu, T. (1961), A statistical study on the occurrence of aftershocks, *Geophys. Mag.*, *30*(4), 521–605.
Utsu, T. (1999), Representation and analysis of the earthquake size distribution: A historical review and some new approaches, *Pure Appl. Geophys.*, *155*(2–4), 509–535, doi:10.1007/s000240050276.
Utsu, T., Y. Ogata, and R. S. Matsu'ura (1995), The centenary of the Omori formula for a decay law of aftershock activity, *J. Phys. Earth*, *43*(1), 1–33, doi:10.4294/jpe1952.43.1.
Vasco, D. W., J. Rutqvist, A. Ferretti, A. Rucci, F. Bellotti, P. Dobson, C. Oldenburg, J. Garcia, M. Walters, and C. Hartline (2013), Monitoring deformation at the Geysers Geothermal Field, California using C-band and X-band interferometric synthetic aperture radar, *Geophys. Res. Lett.*, *40*, 2567–2572, doi:10.1002/grl.50314.
Vidale, J. E., and P. M. Shearer (2006), A survey of 71 earthquake bursts across southern California: Exploring the role of pore fluid pressure fluctuations and aseismic slip as drivers, *J. Geophys. Res.*, *111*, B05312, doi:10.1029/2005JB004034.
Waldhauser, F., and D. P. Schaff (2008), Large-scale relocation of two decades of Northern California seismicity using cross-correlation and double-difference methods, *J. Geophys. Res.*, *113*, B08311, doi:10.1029/2007JB005479.
Walter, A. W., and C. S. Weaver (1980), Seismicity of the Coso Range, California, *J. Geophys. Res.*, *85*(B5), 2441–2458, doi:10.1029/JB085iB05p02441.
Wei, S., et al. (2011), Superficial simplicity of the 2010 El Mayor-Cucapah earthquake of Baja California in Mexico, *Nat. Geosci.*, *4*(9), 615–618, doi:10.1038/ngeo1213.
Weingarten, M., S. Ge, J. W. Godt, B. A. Bekins, and J. L. Rubinstein (2015), High-rate injection is associated with the increase in U.S. mid-continent seismicity, *Science*, *348*(6241), 1336–1340, doi:10.1126/science.aab1345.
Wessel, P., W. H. F. Smith, R. Scharroo, J. Luis, and F. Wobbe (2013), Generic Mapping Tools: Improved version released, *Eos Trans. AGU*, *94*(45), 409–410, doi:10.1002/2013EO450001.

Woessner, J. (2005), Assessing the quality of earthquake catalogues: Estimating the magnitude of completeness and its uncertainty, *Bull. Seismol. Soc. Am.*, *95*(2), 684–698, doi:10.1785/0120040007.

Younker, L. W., P. W. Kasameyer, and J. D. Tewhey (1982), Geological, geophysical, and thermal characteristics of the Salton Sea Geothermal Field, California, *J. Volcanol. Geotherm. Res.*, *12*(3–4), 221–258, doi:10.1016/0377-0273(82)90028-2.